

# Scale-variant Topological Information for Characterizing Complex Networks

Quoc Hoan Tran<sup>1</sup>, Van Tuan Vo<sup>1</sup>, and Yoshihiko Hasegawa<sup>1</sup>

<sup>1</sup> *Department of Information and Communication Engineering  
Graduate School of Information Science and Technology  
The University of Tokyo, Tokyo 113-8656, Japan*

December 15, 2024

## Abstract

Real-world networks are difficult to characterize due to the variation of topological scales, the non-dyadic complex interactions, and fluctuations. Here, we propose a general framework to address these problems via a methodology grounded in topology data analysis. By observing the diffusion process on the network at single specified time scale, we can map network nodes to a point cloud which contains the topological information of the network at a single scale. We then calculate the point clouds constructed over variable time scales, which provide scale-variant topological information and confer the deep understanding of network structure and functionality. Experiments on synthetic and real-world data demonstrate the effectiveness of our framework in identifying network models, classifying real-world networks, and detecting transition points in time-evolving networks. Our work presents a unified analysis which is potentially applicable to more complicated network structures such as multilayer and multiplex networks.

Characterizing the structure of complex networks is the most fundamental issue to decipher myriads of dynamics on the network. The network anatomy is quite relevant to phenomena occurring on networks such as the spread of information and epidemic, the robustness and stability under attack. Considerable applications have been of great interest in the literature. These applications include control and prediction of dynamics patterns on networks<sup>1-3</sup>, quantification of the structural and functional similarity of biological networks<sup>4-6</sup>, and detection of transition points in time-evolving networks<sup>7-9</sup>.

In practice, the structure of real-world networks is inherently difficult to characterize. Firstly, real-world networks have complex patterns that are reflected in various topological scales<sup>10-12</sup> (Fig. 1a). In revealing these patterns, the conventional statistical measures<sup>13,14</sup> and methods<sup>10,15-18</sup> remain ill-defined, as evidenced by the lack of representing the variation of topological scales. Secondly, the real-world network is a representation of the complex system having dyadic and non-dyadic interactions<sup>19-21</sup> (Fig. 1b). However, the majority of current methods to characterize complex networks only focus on the dyadic interactions between nodes such as the existence of pairwise edges or the paths connected by succession edges. Thirdly, real-world networks often suffer from fluctuation caused by external factors<sup>22</sup>. Because of the fluctuation, the quest for unifying principles underlying the topology of networks only emerges in simple idealized models without any additional effect<sup>23-25</sup>. In characterizing the structure of real-world networks, the robust representation under the fluctuation has not been explored.

Our main goal is to propose a general framework addressing abovementioned problems. To reveal the variation of topological scales, we rely on the topological information obtained along with the diffusion process exhibited on the network. When the diffused time  $\tau$  is small, since there is almost no information exchanged among nodes, micro-scale structure is revealed. Increasing  $\tau$  will reflect the meso-scale decomposition of the network until the macro-scale structure is captured at last. At each  $\tau$ , we map network nodes to a point cloud where a group of close points represents the unit of points that easily exchange information in the diffusion process. To capture the non-dyadic interactions, we construct the simplicial complex model<sup>26</sup> from the point cloud. To obtain the robust representation, we use topological data analysis<sup>26-29</sup>, which is a set of computational topology methods to encode the simplicial complex model into the noise-tolerant quantitative features. Observing these features when varying  $\tau$  provides insights into the variation of topological scales, as well as the interplay between structure and dynamics of the network. We therefore construct the scale-variant topological features by regarding  $\tau$  as a variable parameter, rather than as a single fixed value.

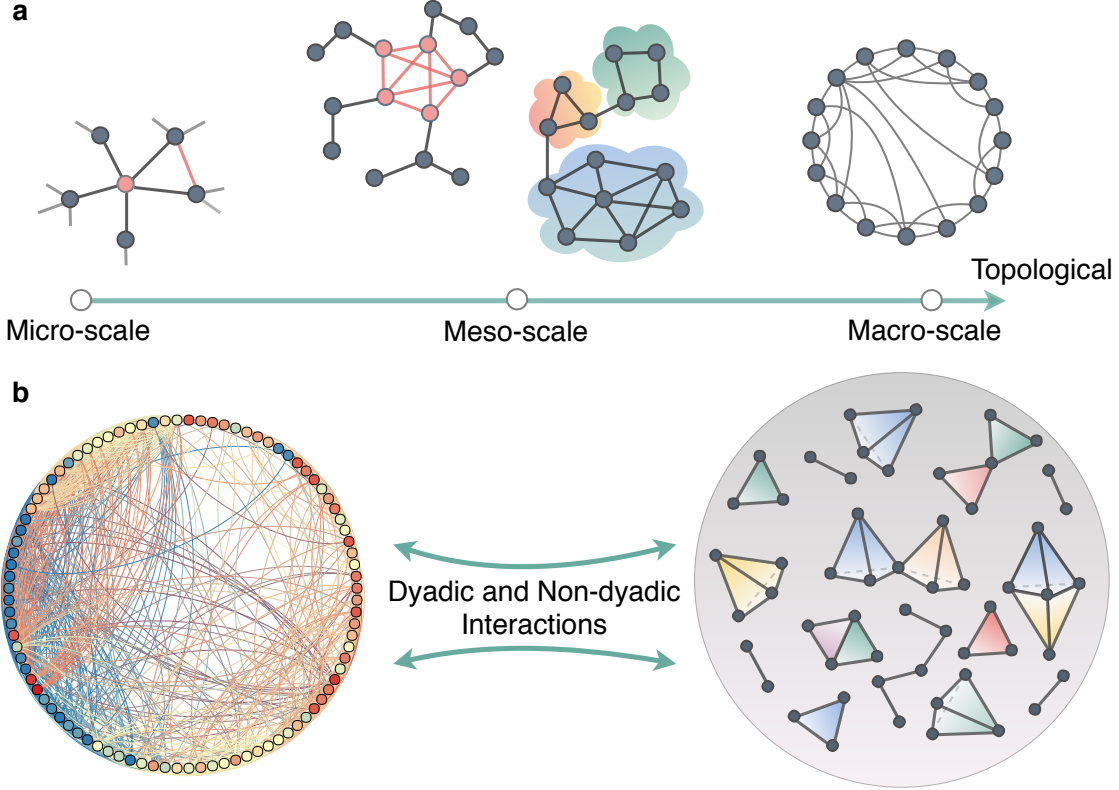


**Figure 1 | Various topological scales and interactions between multiple elements in the complex network.** (a) Complex network can be analyzed at various topological scales ranging from individual nodes (micro-scale), to the whole network (macro-scale). In the intermediate of the two scales, there is meso-scale where we can observe the collective, cores and peripheries patterns. (b) The complex network is a representation of the complex system having dyadic and non-dyadic interactions among elements. Interactions can be represent as simplices such as segments (for dyadic interactions), filled triangles or filled tetrahedrons (for non-dyadic interactions involving three or four elements), and so on.

The proposed framework allows us to study the properties of complex networks that might reflect the variation of topological scales, provide in-depth understanding of the complex interactions, and evaluate the robustness under the fluctuation. Through the analysis on several network models, we demonstrate that our framework can characterize the parameters which are used to generate networks. Interestingly, using the scale-variant topological features, we can distinguish networks generated from different models with empirically better results than other conventional approaches. We further apply our framework to classification of the real-world networks and detection of the transition points in the time-evolving gene regulatory networks. We believe that our study provide a unified analysis of complex networks. Such study has the potential to enable further applications for more complicated network structures such as multilayer and multiplex networks.

## Results

### Scale-variant topological features

We consider an undirected weighted network  $\mathcal{G}$  with  $N$  nodes  $v_1, \dots, v_N$ . We suppose that there is a single random walker, which moves randomly between nodes in continuous time. When the walker is located at  $v_i$ , we assume that the walker moves to the neighbor node  $v_j$  with transition rate  $w_{ij}/k_i$ , where  $w_{ij} \geq 0$  represents the weight of the edge from  $v_i$  to  $v_j$  ( $i, j \in \{1, 2, \dots, N\}$ ) and  $k_i = \sum_{j=1}^N w_{ij}$ . Here,  $w_{ij} = 0$  if there is no edge between  $v_i$  and  $v_j$ . We denote  $p_{\mathcal{G},k}(\tau|i)$  as the probability to find a random walker on  $v_k$  at time  $\tau$  that starts from  $v_i$ . The probability distribution vector  $\mathbf{p}_{\mathcal{G}}(\tau|i) = [p_{\mathcal{G},1}(\tau|i), \dots, p_{\mathcal{G},N}(\tau|i)]$ ,

is given by the solution of the Kolmogorov forward equation

$$\frac{d\mathbf{p}_{\mathcal{G}}(\tau|i)}{dt} = -\mathbf{p}_{\mathcal{G}}(\tau|i)\mathbf{L}_{\mathcal{G}}^{\text{rw}}. \quad (1)$$

Here,  $\mathbf{L}_{\mathcal{G}}^{\text{rw}}$  is the random walk Laplacian whose components  $l_{ij}$  ( $i, j \in \{1, 2, \dots, N\}$ ) are given by

$$l_{ij} = \begin{cases} 1 & \text{if } i = j \text{ and } k_i \neq 0 \\ -1/k_i & \text{if } i \neq j \text{ and } v_i \text{ is adjacent to } v_j \\ 0 & \text{otherwise.} \end{cases} \quad (2)$$

At a specific  $\tau$ , we map nodes of the network  $\mathcal{G}$  to a point cloud of  $N$  points  $\mathbf{p}_{\mathcal{G}}(\tau|1), \dots, \mathbf{p}_{\mathcal{G}}(\tau|N)$ . The shape of this point cloud confers valuable insights into the information exchange process at time  $\tau$ , and the structural property of network  $\mathcal{G}$  at  $\tau$ -scale. As illustrated in Fig. 2a, we consider an undirected network comprising of four clusters in which there are more intra-cluster connections than inter-cluster connections. At each  $\tau$ , the pairwise distances of mapped points of nodes in the same clusters are smaller than the distances between nodes belonging to different clusters. These distances decrease as we increase  $\tau$ . Consequently, the hole patterns in the point cloud appear with different sizes at different groups of points when we vary  $\tau$  (Fig. 2b). Observing the formation of these holes when vary  $\tau$  may reveal the variation of topological scales for the network.

To capture the non-dyadic interactions at each  $\tau$ -scale, we construct the Vietoris–Rips simplicial complex<sup>26,30</sup>, which is a set of simplices built with a non-negative threshold  $\varepsilon$ . In this simplicial complex, each simplex is built over a subset of points if all pairwise distances between points are less than or equal to  $\varepsilon$ . With different  $\varepsilon$  values, we have different simplicial complexes and hence different topological information as the number, position, and size of high dimensional holes such as clusters, loops, and tunnels. We obtain a sequence of embedded simplicial complexes called filtration when increase  $\varepsilon$  (Supplementary Note 1). From the filtration, we can highlight not only simple connectivity but also how network properties change as information propagates.

To encode the hole patterns over the filtration into the quantitative features, we consider the emergence and vanishment of these patterns as topological features for the complex network at  $\tau$ -scale. We use persistent homology theory<sup>26–29,31</sup> to study these topological features and visualize the results through multi-set points in the 2-dimensional *persistence diagram*. In this diagram, each point  $(b, d)$  represents an  $l$ -dimensional hole that appears at  $\varepsilon = b$  (known as the *birth-scale*) and disappears at  $\varepsilon = d$  (known as the *death-scale*) across the filtration (Fig. 2c). Here, connected components are 0-dimensional, loops or tunnels are 1-dimensional holes, and voids are 2-dimensional holes.

We obtain the scale-variant topological features reflecting the variation of topological scales by considering the 2-dimensional persistence diagrams when  $\tau$  varies. We denote  $Dg_{l,\tau}^{(2)}(\mathcal{G})$  as the 2-dimensional persistence diagram of network  $\mathcal{G}$  calculated for  $l$ -dimensional holes at  $\tau$ -scale. We consider  $\tau$  in a pre-defined set  $\mathcal{T} = \{\tau_1, \tau_2, \dots, \tau_K\}$ , where  $0 < \tau_1 < \tau_2 < \dots < \tau_K$  (with  $K$  denoting the set’s size). We define the scale-variant topological features, i.e., the 3-dimensional persistence diagram of  $l$ -dimensional holes for network  $\mathcal{G}$  as  $Dg_l^{(3)}(\mathcal{G}) = \{(b, d, \tau) \mid (b, d) \in Dg_{l,\tau}^{(2)}(\mathcal{G}), \tau \in \mathcal{T}\}$  (Fig. 2d).

To use 3-dimensional persistence diagrams for statistical-learning tasks, we use the positive-definite kernel mapping for such diagrams introduced in ref.<sup>32</sup> (see Methods for the definition of this kernel and its normalized version). We can apply this kernel to detect the transition point in the structure of the collection of networks  $\{\mathcal{G}_1, \mathcal{G}_2, \dots, \mathcal{G}_M\}$ . We consider a collection of diagrams  $\mathcal{D} = \{Dg_1, \dots, Dg_M\}$ , where  $Dg_i$  is a 3-dimensional diagram of network  $\mathcal{G}_i$ . We use the kernel Fisher discriminant ratio<sup>33</sup>  $\text{KFDR}_{M,s}(\mathcal{D})$  calculated from the Gram matrix  $(k_{ij})_{i,j=1,\dots,M}$ , where  $k_{ij}$  is the kernel value between  $Dg_i$  and  $Dg_j$ .  $\text{KFDR}_{M,s}(\mathcal{D})$  is a statistical quantity to measure the dissimilarity between two classes assumptively defined by the two set of data having index before and from  $s$  (Supplementary Note 2). Here, the index  $s$  achieving the maximum of  $\text{KFDR}_{M,s}(\mathcal{D})$  corresponds to the estimated transition point.

## Robustness of scale-variant topological features

We show that the scale-variant topological features, i.e., the 3-dimensional persistence diagrams computed from networks are robust with respect to some perturbations of the network. To formalize such robustness, we first explain the concept of *bottleneck distance* which is a metric structure for comparing persistence diagrams<sup>32</sup>. Given two 3-dimensional persistence diagrams  $E$  and  $F$ , consider all matchings  $\psi$  such that a point on a diagram is matched to a point on the other or to its projection on the plane  $b = d$ .

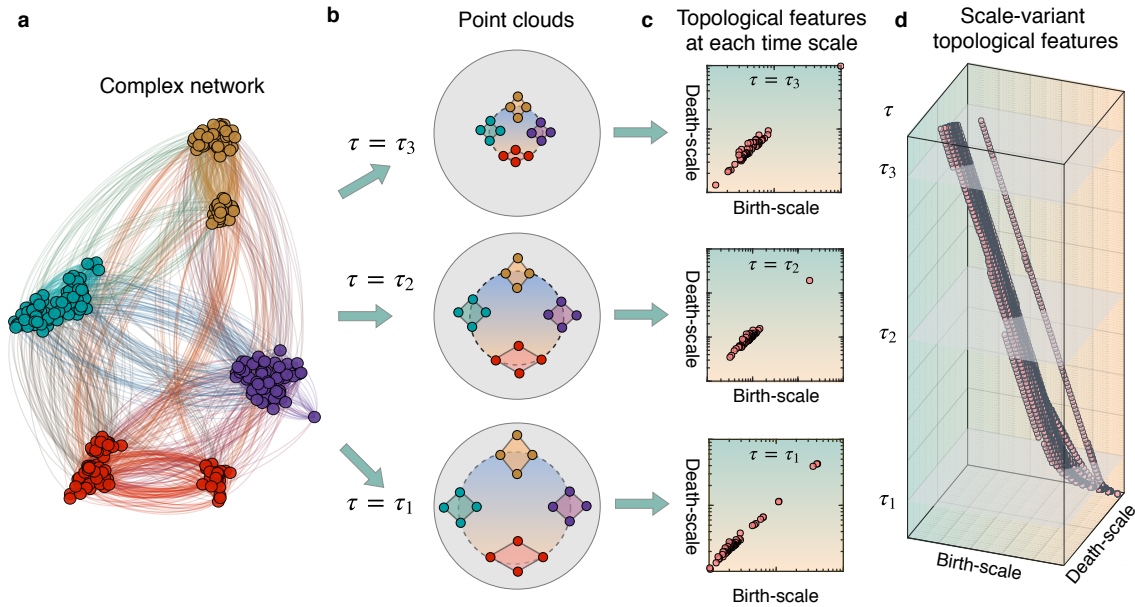


**Figure 2 | Scale-variant topological features reflecting the variation of topological scales.** (a) An undirected network comprising of four clusters in which there are more connections within intra-clusters than between inter-clusters. (b) At each time-scale  $\tau$ , we map nodes to a point cloud in which the distances of mapped points of nodes in the same clusters are smaller than the distances between nodes belonging to the different clusters. These distances decrease when we increase  $\tau$  as  $\tau_1 < \tau_2 < \tau_3$ . The hole patterns in the point cloud such as connected components, loops, and tunnels, appear with different sizes at different group of points when we vary  $\tau$ . (c) The topological features at each  $\tau$  characterize shape of the point cloud. These features are displayed as 2-dimensional persistence diagram for holes appeared at each  $\tau$ -scale. We illustrate here the 2-dimensional persistence diagram for 1-dimensional holes (loops and tunnels). The axes of diagrams are represented at the logarithmic scale. (d) We obtain the scale-variant topological features, i.e., the 3-dimensional persistence diagram, by integrating 2-dimensional diagrams when vary  $\tau$ . The birth-scale and death-scale axes of diagrams are represented at the logarithmic scale.

For each pair  $(\mathbf{p}, \mathbf{q}) \in \psi$  for which  $\mathbf{p} = (b_1, d_1, \tau_1)$  and  $\mathbf{q} = (b_2, d_2, \tau_2)$ , we define *the relative infinity-norm distance* between  $\mathbf{p}$  and  $\mathbf{q}$  as  $d_\xi^{(\infty)}(\mathbf{p}, \mathbf{q}) = \max(|b_1 - b_2|, |d_1 - d_2|, \xi|\tau_1 - \tau_2|)$ . Here,  $\xi$  is a positive rescaling coefficient introduced to adjust the scale difference between the point-wise distance and time. The bottleneck distance,  $d_{B,\xi}^{(3)}(E, F)$ , is defined as the infimum of the longest matched relative infinity-norm distance over all matchings,  $\psi$ :

$$d_{B,\xi}^{(3)}(E, F) = \inf_{\psi} \max_{(\mathbf{p}, \mathbf{q}) \in \psi} d_\xi^{(\infty)}(\mathbf{p}, \mathbf{q}). \quad (3)$$

If two undirected networks  $\mathcal{G}$  and  $\mathcal{H}$  with the same number  $N$  of nodes are given, we show that the bottleneck distance between  $Dg_l^{(3)}(\mathcal{G})$  and  $Dg_l^{(3)}(\mathcal{H})$  is bounded from above by the matrix 2-norm of the difference between their random walk Laplacian matrices

$$d_{B,\xi}^{(3)}(Dg_l^{(3)}(\mathcal{G}), Dg_l^{(3)}(\mathcal{H})) \leq 2\tau_K \|\mathbf{L}_{\mathcal{G}}^{\text{rw}} - \mathbf{L}_{\mathcal{H}}^{\text{rw}}\|_2. \quad (4)$$

Here,  $\|\mathbf{A}\|_2$  is the matrix 2-norm of matrix  $\mathbf{A}$  induced by the euclidean vector norm and defined as  $\|\mathbf{A}\|_2 = \max_{\|\mathbf{x}\|_2=1} \|\mathbf{A}\mathbf{x}\|_2$ . In Supplementary Note 3, we present our proof for Eq. (4), which is based on the stability properties of 2-dimensional persistence diagrams<sup>34</sup> and the sensitivity of the matrix exponential<sup>35</sup>.

The inequality of Eq. 4 states the following important property. Our scale-variant topological features are robust with respect to the perturbation applied to the random walk Laplacian matrix of the network. Therefore, these features can be used as discriminative features to characterize networks.

## Understanding variations of the parameters of network models

Using network models listed below, we investigate how the scale-variant topological features reflect variations of the parameters of network models. We generate networks from Girvan–Newman<sup>36</sup> (GN), Lancichinetti–Fortunato–Radicchi<sup>37,38</sup> (LFR), Erdős–Rényi<sup>39</sup> (ER), Watts–Strogatz<sup>40</sup> (WS), Lancichinetti–Fortunato–Radicchi with hierarchical structure<sup>17</sup> (LFR–H), and Sales–Pardo<sup>16</sup> (SP) models (see Methods for the description). We focus on model parameters which represent the topological scale of these networks. These parameters are the ratio  $r$  between the probability of inter-community links ( $p_{\text{out}}$ ) and intra-community links ( $p_{\text{in}}$ ) in GN model, the mixing rate  $\mu$  in LFR model, the rewiring probability  $\beta$  in WS model, the pair-link probability  $p_{\text{link}}$  in ER model, the mixing rate  $\mu_{\text{macro}}$  for macro communities in LFR–H model, and  $\rho$  which quantifies the separations between topological scales in SP model. We generate a number of network realizations at each value of the parameters, then observe the variation in the kernel space when these parameters vary.

We compute the 3-dimensional persistence diagrams for 1-dimensional holes with time-scale values  $\tau_1 = 1, \tau_2 = 2, \dots, \tau_{100} = 100$ . Figure 3 shows the 3-dimensional principal-components projections from the kernel space of each model, where points with different colors represent the networks generated from different values of the parameters. In ER, WS, LFR–H, and SP models, the scale-variant topological features reflect the variation of the parameters associated with the topological scales because points located at different positions have different colors (Fig. 3c-f). In GN and LFR models, there are variations in topological scales of the network as  $r$  ( $= p_{\text{out}}/p_{\text{in}}$ ) and  $\mu$  vary from 0 (four separate groups) to 1 (a purely random graph). We detect the transition point for the series of networks obtained when increasing  $r$  as  $r_1 = 0.01, r_2 = 0.02, \dots, r_{100} = 1.0$  (GN model) and  $\mu$  as  $\mu_1 = 0.01, \mu_2 = 0.02, \dots, \mu_{100} = 1.0$  (LFR model). We obtain the phase transition at  $r = 0.11$  (Supplementary Fig. 1) and  $\mu = 0.26$  (Supplementary Fig. 2). These values correspond to boundaries between identifiable, where parameters can be identified from the kernel space, and non-identifiable phases (Fig. 3a,b).

## Identification of network models

To evaluate the effectiveness of the scale-variant topological features, we demonstrate that the features can distinguish networks generated from different models even if they have similar global statistical measures. We focus on the GN, LFR and WS models with the same parameter settings in the previous section. In each model, we generate 10 networks for each value of the model parameter. We consider the configuration model<sup>41</sup> which generates random networks (known as the *configuration networks*) having the same sequences of node degrees with a given network. We generate 1000 networks from the GN model (GN–original), 1000 networks from the LFR model (LFR–original), and 1010 networks from the WS model (WS–original), with their corresponding configuration networks denoted as GN–config,

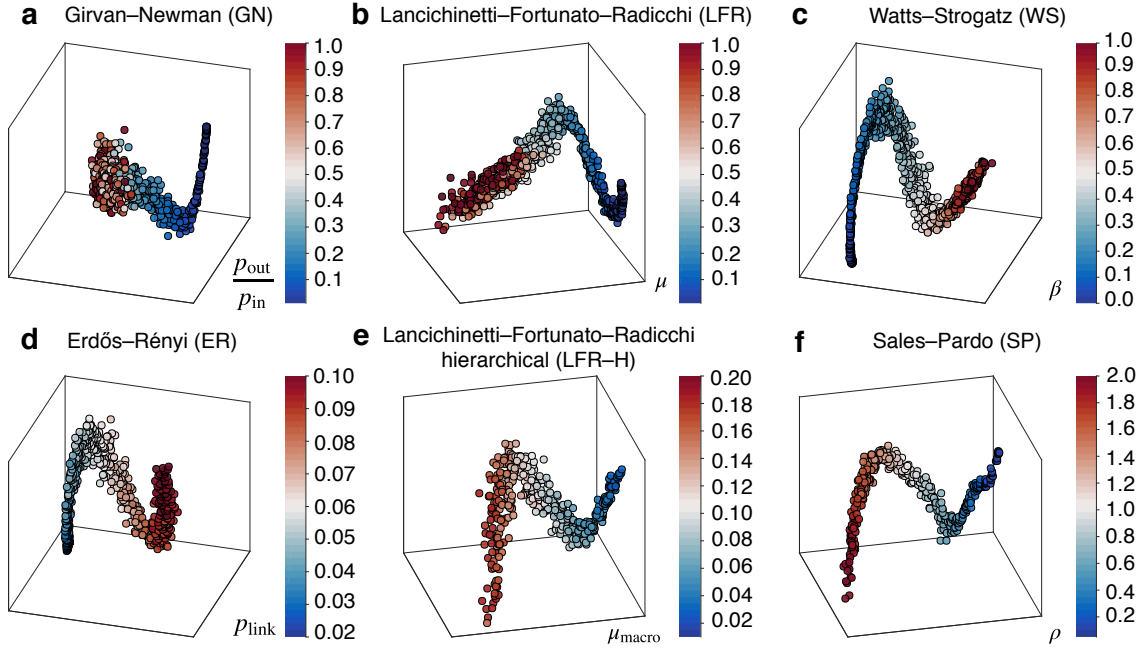


**Figure 3 | The kernel principal components projection of scale-variant topological features for 1-dimensional holes in each network model.** The different colors represent data generated from different values of the model parameters. We generate networks from (a) Girvan–Newman (GN), (b) Lancichinetti–Fortunato–Radicchi (LFR), (c) Watts–Strogatz (WS), (d) Erdős–Rényi, (e) Lancichinetti–Fortunato–Radicchi hierarchical (LFR–H), and (f) Sales–Pardo (SP) models. We vary the parameters for these models as  $r = p_{\text{out}}/p_{\text{in}} = 0.01, 0.02, \dots, 1.0$  (GN),  $\mu = 0.01, 0.02, \dots, 1.0$  (LFR),  $\beta = 0.00, 0.01, \dots, 1.0$  (WS),  $p_{\text{link}} = 0.020, 0.021, \dots, 0.1$  (ER), and  $\mu_{\text{macro}} = 0.01, 0.02, \dots, 0.2$  (LFR–H),  $\rho = 0.05, 0.10, \dots, 2.0$  (SP).

LFR-config, and WS-config, respectively. We compute the 3-dimensional persistence diagrams for 1-dimensional holes of these networks with time-scale values  $\tau_1 = 1, \tau_2 = 2, \dots, \tau_{100} = 100$ . We calculate kernel for these diagrams, then perform the 3-dimensional principal-components projections from the kernel space (Fig. 4a). Here, points with different colors represent the networks generated from different models. In Fig. 4a, points appear to be distinguishable by their colors.

We quantify to what extent the proposed framework identifies networks generated from different models. We perform the scale-variant method which uses the scale-variant topological features to classify networks into six labels as GN-original, LFR-original, WS-original, and GN-config, LFR-config, and WS-config. For 10 networks generated at each value of the model parameters, we randomly split into five networks for training and the remainings for testing. We apply the support vector machine<sup>42</sup> for classification in the normalized kernel space. Figure 4b shows the average normalized confusion matrix over 100 random splits where row and column labels are predicted and true labels, respectively. Using the scale-variant topological features, we can identify almost perfectly networks which are generated from different models. Networks with GN-original, LFR-original, and WS-original labels can be identified with about 99% accuracy. Interestingly, the features allow us to capture the difference between networks and their configuration networks; even they have the same sequences of node degrees. It shows considerably high accuracy for GN-config (94%), LFR-config (99%), and WS-config (96%). This result indicates that the scale-variant topological features appear to reflect the essential behaviors of network models.

To highlight the benefits of scale-variant method, we compare it with other conventional methods. These are the method using the common statistical measures extracted from the network (see Methods), the graph kernels to measure the similarity between networks, and the methods based on the topological features calculated at a fixed topological scale. In Supplementary Note 4, we describe the graph kernels which are based on random walks (KStepRW, GeometricRW, ExponentialRW)<sup>43,44</sup>, paths (Shortest-Path<sup>45</sup>), limited-sized subgraphs (Graphlet<sup>46</sup>), and subtree patterns (Weisfeiler-Lehman<sup>47</sup>). The implementations of these graph kernels can be found in ref.<sup>48</sup>. We consider two variants of topological features calculated from average distance matrix  $\Delta_{\text{avg}} = (1/K) \sum_{i=1}^K \Delta_{\tau_i}$  (scale-average), and average normalized distance matrix  $\tilde{\Delta}_{\text{avg}} = (1/K) \sum_{i=1}^K \tilde{\Delta}_{\tau_i}$  (scale-norm-average). Here,  $\Delta_{\tau_i}$  is the distance matrix of pairwise euclidean distances between points  $\mathbf{p}_G(\tau_i|1), \dots, \mathbf{p}_G(\tau_i|N)$  (see Supplementary Note 1 and Supplementary Fig. 1), and  $\tilde{\Delta}_{\tau_i}$  is obtained by dividing  $\Delta_{\tau_i}$  by its maximum element<sup>49</sup>.

We compute the average classification accuracy over 100 random splits at different proportions of training data. Figure 4c highlights the significant advantages of the scale-variant method. The accuracy of the scale-variant method shows notably higher values compare with other methods. Even with the small size of training data set, e.g., only 10% of all data, the scale-variant method can achieve about 97% of accuracy. In contrast, the accuracies of the other methods are not larger than 84%. Remarkably, the accuracy of the scale-variant method does not change over a wide range of proportion for training data. These results demonstrate the effectiveness and reliability of using the scale-variant topological features in comparison with the conventional methods to capture the differences between network structures.

## Classification of real-world network data

We apply scale-variant topological features to real-world datasets of bioinformatics networks (MUTAG, BZR, COX2, DHFR, FRANKENSTEIN, PROTEINS, NCI1, NCI109) and social networks (IMDB-BINARY, IMDB-MULTI). All networks are available at ref.<sup>50</sup> (see Methods for the description). The bioinformatics datasets have the discrete labels for nodes that may be useful but we only use the connectivity information to evaluate the classification methods. We compute 3-dimensional persistence diagrams with time-scale values  $\tau_1 = 1, \dots, \tau_{50} = 50$  and use the sum kernel of normalized kernel for 0-dimensional holes and 1-dimensional holes.

We compare the scale-variant method with the methods using common statistical measures and other graph kernel methods, the scale-average and scale-norm-average methods described in the previous section. Table 1 presents the average accuracies along with their standard deviations over 100 train-test splits. In each split of the dataset, we randomly take 80% of networks for training and the remainings for testing. In the Table 1, the best and second-best average accuracy scores of each dataset are colored in dark pink and light pink, respectively. The scale-variant method outperforms all the other methods on average. For seven out of the ten datasets, it offers the best results, and offers the second-best for two more. This result suggests that the method based on the scale-variant topological features can be considered to be an effective approach for classifying real-world network data.

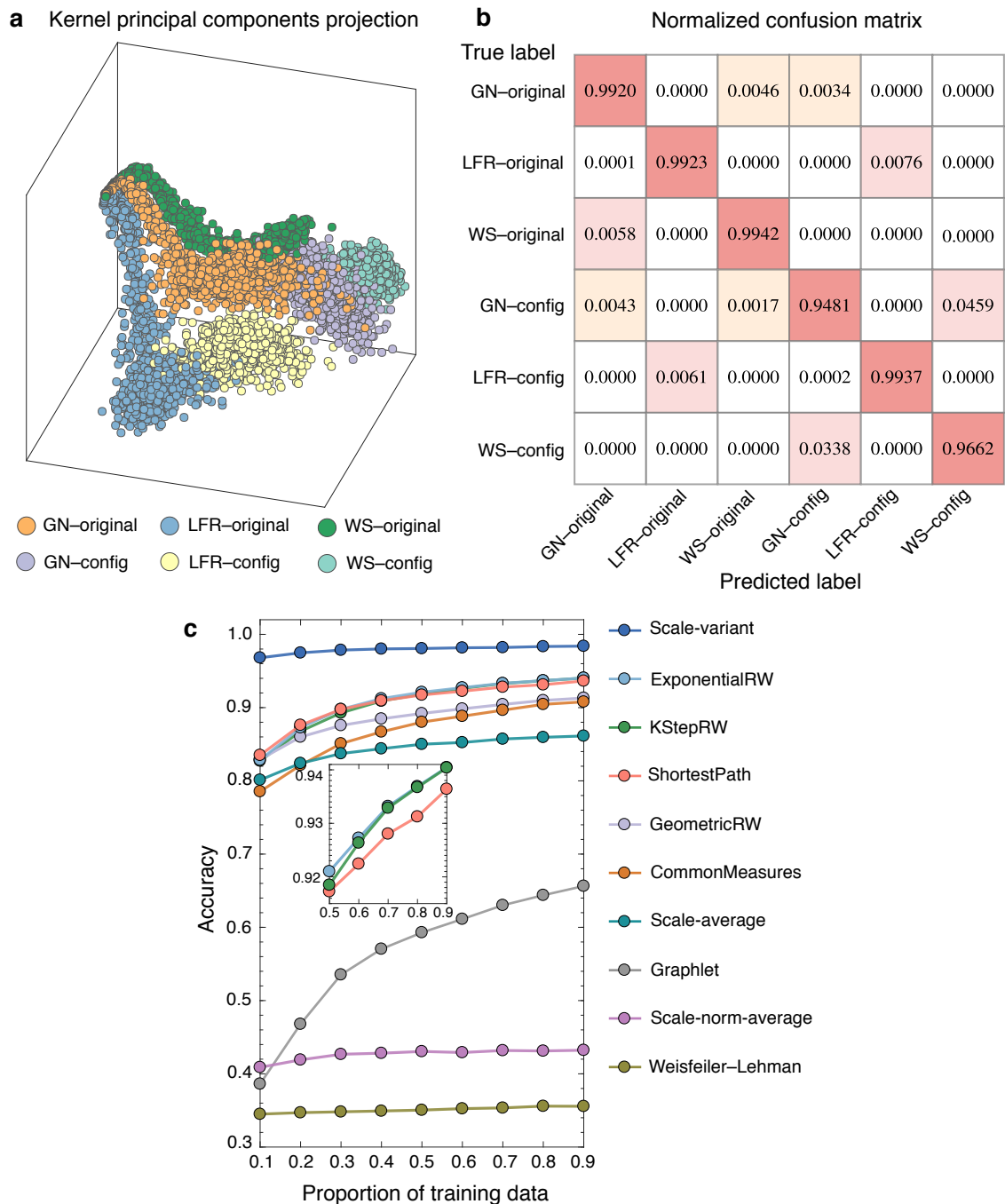


**Figure 4 | Scale-variant topological features applied to classify networks generated from different models.** We generate 1000 networks from GN model, 1000 networks from LFR model, and 1010 networks from WS model, with labels as GN-original, LFR-original, and WS-original, respectively. We generate their corresponding configuration networks, with labels as GN-config, LFR-config, and WS-config, respectively. Using the scale-variant topological features, we perform the scale-variant method to classify total 6020 networks into these six labels. **(a)** The kernel principal components projection of scale-variant topological features for these networks. The different colors represent networks generated from different models. **(b)** The normalized confusion matrix of the scale-variant method over 100 random train-test splits of data. For 10 networks generated at each value of the model parameters, we randomly split into five networks for training and the remains for testing. **(c)** Comparison of classification methods in the average accuracies over 100 random train-test splits at each different proportion of training data. The inset highlights the accuracies of the ExponentialRW, KStepRW, and ShortestPath method when the proportion of the training data goes from 0.5 to 0.9.

**Table 1** | The average and standard deviation (mean $\pm$ sd) for the classification accuracy (%) of datasets MUTAG, BZR, COX2, DHFR, FRANKENSTEIN, PROTEINS, NCI1, NCI109, IMDB-BINARY, and IMDB-MULTI. In each dataset, the best and second-best scores are colored in dark pink and light pink, respectively.

Method	MUTAG	BZR	COX2	DHFR	FRANKENSTEIN	PROTEINS	NCI1	NCI109	IMDB-BINARY	IMDB-MULTI
Scale-variant	88.3 $\pm$ 5.1	86.8 $\pm$ 3.0	78.4 $\pm$ 1.8	78.4 $\pm$ 2.9	69.4 $\pm$ 1.5	72.6 $\pm$ 2.0	71.6 $\pm$ 1.3	70.5 $\pm$ 1.2	72.9 $\pm$ 3.0	50.3 $\pm$ 2.5
Graphlet	83.4 $\pm$ 5.7	78.2 $\pm$ 0.4	77.7 $\pm$ 0.0	61.2 $\pm$ 0.0	57.0 $\pm$ 0.7	71.8 $\pm$ 2.1	62.9 $\pm$ 1.5	62.8 $\pm$ 1.4	59.0 $\pm$ 3.5	41.0 $\pm$ 2.2
KStepRW	82.7 $\pm$ 5.8	85.6 $\pm$ 3.1	76.9 $\pm$ 2.0	75.7 $\pm$ 3.1	69.1 $\pm$ 1.4	73.4 $\pm$ 2.4	67.6 $\pm$ 1.5	68.1 $\pm$ 1.6	61.0 $\pm$ 3.6	45.6 $\pm$ 2.5
GeometricRW	82.8 $\pm$ 5.9	84.7 $\pm$ 3.2	77.1 $\pm$ 1.9	75.4 $\pm$ 3.0	68.8 $\pm$ 1.4	72.1 $\pm$ 2.2	65.6 $\pm$ 1.5	65.5 $\pm$ 1.5	67.5 $\pm$ 3.6	47.9 $\pm$ 2.7
ExponentialRW	82.9 $\pm$ 5.8	86.2 $\pm$ 3.2	76.9 $\pm$ 2.0	75.9 $\pm$ 3.3	68.7 $\pm$ 1.4	72.3 $\pm$ 2.3	65.4 $\pm$ 1.5	65.7 $\pm$ 1.6	66.4 $\pm$ 3.3	47.4 $\pm$ 2.6
ShortestPath	82.1 $\pm$ 6.1	84.6 $\pm$ 3.1	77.1 $\pm$ 1.7	74.7 $\pm$ 3.4	66.3 $\pm$ 1.5	72.4 $\pm$ 2.2	64.9 $\pm$ 1.5	64.7 $\pm$ 1.4	58.0 $\pm$ 3.6	43.9 $\pm$ 2.6
Weisfeiler-Lehman	85.2 $\pm$ 5.4	84.9 $\pm$ 2.8	77.4 $\pm$ 1.5	77.2 $\pm$ 3.3	71.5 $\pm$ 1.4	72.6 $\pm$ 2.2	71.0 $\pm$ 1.3	71.6 $\pm$ 1.5	61.2 $\pm$ 2.9	47.8 $\pm$ 2.3
CommonMeasures	84.7 $\pm$ 4.8	82.8 $\pm$ 1.8	77.7 $\pm$ 0.0	69.7 $\pm$ 3.0	63.7 $\pm$ 1.3	75.6 $\pm$ 2.2	67.4 $\pm$ 1.5	67.1 $\pm$ 1.4	71.6 $\pm$ 2.7	45.4 $\pm$ 2.4
Scale-average	85.9 $\pm$ 5.7	79.1 $\pm$ 1.3	77.7 $\pm$ 0.0	67.3 $\pm$ 3.1	62.7 $\pm$ 1.1	70.9 $\pm$ 1.9	66.8 $\pm$ 1.6	66.1 $\pm$ 1.6	71.0 $\pm$ 2.8	33.3 $\pm$ 0.0
Scale-norm-average	85.3 $\pm$ 6.0	81.1 $\pm$ 1.6	77.7 $\pm$ 0.0	61.2 $\pm$ 0.0	60.4 $\pm$ 1.3	71.7 $\pm$ 1.9	65.3 $\pm$ 1.8	65.6 $\pm$ 1.4	70.8 $\pm$ 2.8	46.0 $\pm$ 2.3

## Detection of transition points in time-evolving gene regulatory network

Using our scale-variant topological features, we detect transition points of *Drosophila Melanogaster* gene regulatory network. We use a genome-wide microarray profiling which revealed the expression patterns of 4028 genes simultaneously measured during the development of *Drosophila Melanogaster*<sup>51</sup>. Based on ref.<sup>52</sup>, 66 time points are chosen from the full developmental cycle, i.e, the embryonic stage (time points 1–30), the larval stage (time points 31–40), the pupal state (time points 41–58), and the adulthood stage (time points 59–66). Along with ref.<sup>53</sup>, the time-evolving gene regulatory networks are constructed for 588 genes which are known to be related to developmental process based on their gene ontologies. For each gene regulatory network, we compute the 3-dimensional persistence diagrams for 1-dimensional holes with time-scale values  $\tau_1 = 1, \dots, \tau_{100} = 100$ . Supplementary Fig. 3–5 depicts the 3-dimensional persistence diagrams at full time points ranging from  $t = 1$  to  $t = 66$ .

We detect the transition point in a window of consecutive time-points spanning between two consecutive states. In each window, we identify the transition time point  $t_c$  which is the time-index achieving the maximum value of the kernel Fisher discriminant ratio. From the embryonic stage to the larval stage (Fig. 5a), we obtain the transition time points as  $t_c = 28$  and  $t_c = 31$ , which are relatively close to the experimentally known transition time point  $t = 31$  from the profiling. From the larval stage to the pupal stage (Fig. 5b), and from the pupal stage to the adulthood stage (Fig. 5c), we obtain the transition time points as  $t_c = 41$  and  $t_c = 59$ , respectively. These points agree with experimentally known transition time points. Our results suggest that our framework can detect transition points in dynamical networks using network structures alone.

## Discussion

The main goal of this study was to represent the variation of topological scales, capture the non-dyadic interactions, and provide the robustness against noise in characterizing complex networks. Here we proposed a general framework in constructing the scale-variant topological features from diffusion process exhibited on the network. We derived a strong mathematical guarantee for the robustness of these features with respect to perturbations applied to the network. Through several experiments, we provided empirical evidence for the effectiveness of these features in applications such as classification and transition points detection. Our results suggest that the observation of topological features induced from the network dynamics over variant scales can characterize the structure and functionality of networks.

The scale-variant topological features in our framework does not directly correspond to common statistical measures which are constructed from dyadic interactions between nodes at a single fixed topological scale. Our features are rather encoding information of both dyadic and non-dyadic interaction on networks at variant topological scales. In the classification of networks, our features act as strong and essential factors to identify networks. As an application in time-evolving gene regulatory networks, our framework can detect the transition points between the developmental stages of *Drosophila Melanogaster*. These transition points agree with those obtained from the experimental results on the profiling of *Drosophila Melanogaster*. Therefore, from different perspectives than previous approaches, our findings indicate that understanding the variation of topological scales, and non-dyadic interactions can provide important insights into the behavior of complex systems.

In our experiments, the scale-variant topological features are constructed from 0-dimensional and 1-dimensional holes. In principle, we can compute the features from higher dimensional holes which represent non-dyadic interactions involving more number of nodes in each interaction. However, if we

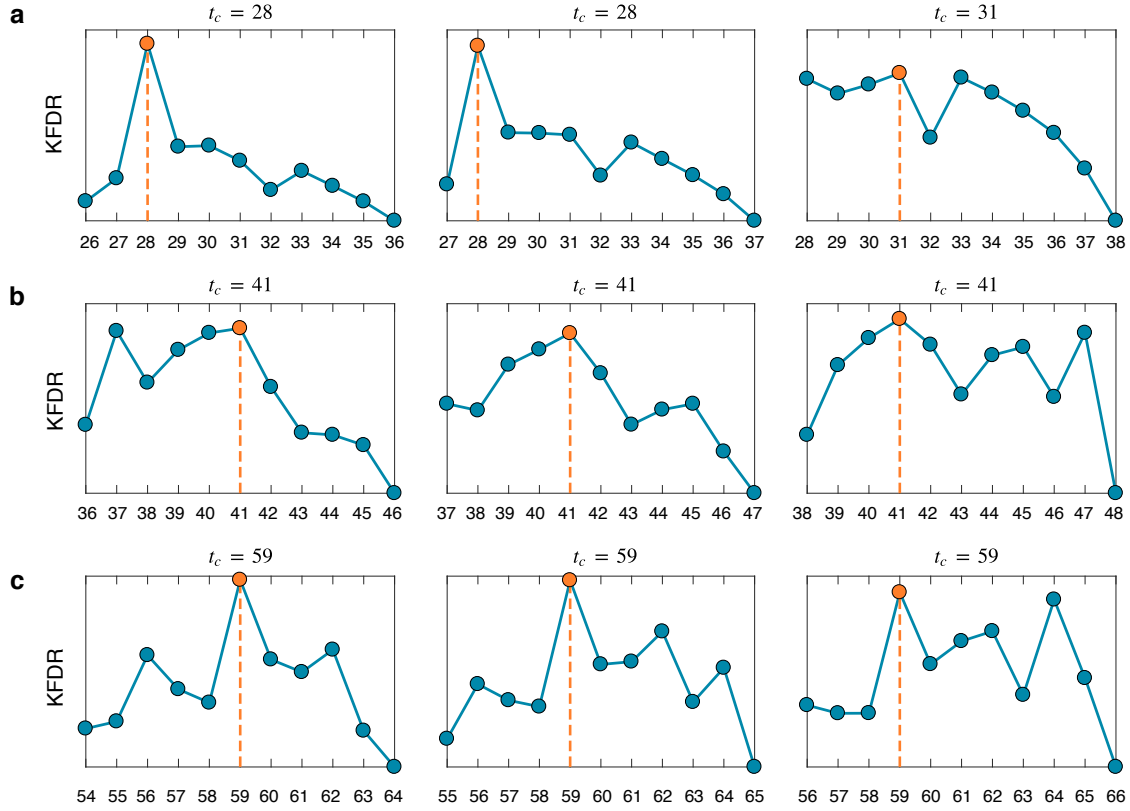


**Figure 5 | Kernel Fisher discriminant ratio (KFDR) calculated from 3-dimensional persistence diagrams of time-evolving *Drosophila Melanogaster* gene regulatory networks.** We detect the transition time points in the windows of 11 time points spanning from different developmental stages. In each window, the transition time point  $t_c$  is the time-index of maximum KFDR value marked with the orange point. **(a)** The windows from the embryonic stage to the larval stage as 26  $\rightarrow$  36 ( $t_c = 28$ ), 27  $\rightarrow$  37 ( $t_c = 28$ ), and 28  $\rightarrow$  38 ( $t_c = 31$ ). **(b)** The windows from the larval stage to the pupal stage as 36  $\rightarrow$  46 ( $t_c = 41$ ), 37  $\rightarrow$  47 ( $t_c = 41$ ), 38  $\rightarrow$  48 ( $t_c = 41$ ). **(c)** The windows from the pupal stage to the adulthood stage as 54  $\rightarrow$  64 ( $t_c = 59$ ), 55  $\rightarrow$  65 ( $t_c = 59$ ), and 56  $\rightarrow$  66 ( $t_c = 59$ ).

want to investigate the features from high dimensional holes, the Vietoris–Rips filtration used in our study can consist of a large number of simplices. More precisely, to consider  $l$ -dimensional holes, the Vietoris–Rips filtration has size  $O(N^{l+1})$  of the number of simplices. This observation implies the difficulty of using the features from  $l$ -dimensional holes ( $l \geq 2$ ) for networks with a large number of nodes  $N$ . However, as demonstrated in this paper, we found that it is sufficient in practical applications to use  $l$ -dimensional holes with  $l = 0, 1$ . Furthermore, one can replace the Vietoris–Rips filtration by the Witness filtration<sup>54</sup>, or the approximation of the Vietoris–Rips filtration<sup>55</sup> for more efficient computations.

Our work is expected to become a unified analysis of complex networks. This work opens up new possibilities for the design of more effective algorithms in network science. Such possibilities include the investigation in more complicated network structures. For instance, we can employ the proposed framework to study different aspects of multiplex networks, or apply to the structural reducibility of a multilayer network while preserving its dynamics and function.

## Methods

**Network models.** We describe network models used in our experiments.

GN is a particular case of the planted  $l$ -partition model. We use the network with 128 nodes partitioned into 4 communities of size 32 and the average degree of 16. In GN model, we focus on the ratio  $r$  between the probability of inter-community links ( $p_{\text{out}}$ ) and intra-community links ( $p_{\text{in}}$ ). We vary  $r = p_{\text{out}}/p_{\text{in}} = 0.01, 0.02, \dots, 1.0$  and generate 10 random realizations of network for each value of  $r$ .

LFR is a model which generates network with a priority known communities, and both node degrees and community size follow the power-law distribution. We focus on the mixing rate  $\mu$  ( $0 \leq \mu \leq 1.0$ ), where each node shares a fraction  $1 - \mu$  of links with nodes inside its community and a fraction of  $\mu$  with the nodes outside its community. For the standard LFR model, we set the number of nodes as 128, average and maximum degrees as 16 and 32, and minimum and maximum community size as 16 and 32. The power-law exponent coefficients for the degree distribution, community size distribution, and weights distribution are  $t_1 = -2, t_2 = -1$  and  $t_3 = 1$ , respectively. We vary the mixing rate as  $\mu = 0.01, 0.2, \dots, 1.0$ , and use the program provided in ref.<sup>37</sup> to generate 10 random realizations of network for each value of  $\mu$ .

We generate networks from WS rewiring model of 128 nodes and rewiring probability  $\beta = 0.00, 0.01, \dots, 1.0$ , with 10 random realizations for each value of  $\beta$ .

ER model is a classical model which generates random networks. We set the number of nodes as 128, vary the pair-link probability  $p_{\text{link}} = 0.020, 0.021, \dots, 0.1$ , and generate 10 random realizations of networks for each value of  $p_{\text{link}}$ .

We generate networks from LFR–H model with hierarchical structure of communities. The number of nodes is 300, minimum and maximum for micro community size are 10 and 50, minimum and maximum for macro community size are 20 and 80, and average and maximum degrees are 20 and 25, respectively. The power-law exponent for the degree distributions and community size distribution are the same as the standard LFR model. We keep the mixing rate for micro communities as  $\mu_{\text{micro}} = 0.16$ , and vary the mixing value for macro communities as  $\mu_{\text{macro}} = 0.01, 0.02, \dots, 0.2$  with 20 random realizations for each value of  $\mu_{\text{macro}}$ .

Finally, SP is a model which generates hierarchical networks with 640 nodes, and three community structure nested in one another. There are 64 communities of 10 nodes at small scale level, 16 communities of 40 nodes at medium scale level, and 4 communities of 160 nodes at large scale level. There are two parameters; the average degree  $\bar{k}$  which represents the density of the network, and  $\rho$  which quantifies the separations between the three scales. We keep  $\bar{k} = 16$ , vary the parameter  $\rho = 0.05, 0.10, \dots, 2.0$ , and use the program provided in ref.<sup>18</sup> to generate 10 random realizations of networks at each value of  $\rho$ .

**Kernel method for 3-dimensional persistence diagrams.** Given a positive bandwidth  $\sigma$  and the positive rescaling coefficient  $\xi$  introduced to adjust the scale difference between the point-wise distance and time, we define the kernel  $k_{\sigma, \xi}$  between two 3-dimensional persistence diagrams,  $E$  and  $F$ , as

$$k_{\sigma, \xi}(E, F) = \frac{1}{\sigma\sqrt{2\pi}} \sum_{\mathbf{p} \in E, \mathbf{q} \in F} \left( e^{-\frac{d_{\xi}^2(\mathbf{p}, \mathbf{q})}{2\sigma^2}} - e^{-\frac{d_{\xi}^2(\mathbf{p}, \bar{\mathbf{q}})}{2\sigma^2}} \right), \quad (5)$$

where  $d_{\xi}^2(\mathbf{p}, \mathbf{q}) = |b_1 - b_2|^2 + |d_1 - d_2|^2 + \xi^2|\tau_1 - \tau_2|^2$ ,  $d_{\xi}^2(\mathbf{p}, \bar{\mathbf{q}}) = |b_1 - d_2|^2 + |d_1 - b_2|^2 + \xi^2|\tau_1 - \tau_2|^2$ , with  $\mathbf{p} = (b_1, d_1, \tau_1)$  and  $\mathbf{q} = (b_2, d_2, \tau_2)$ ,  $\bar{\mathbf{q}} = (d_2, b_2, \tau_2)$ . The normalized version of the kernel is defined by the normalization  $k_{\sigma, \xi}(E, F) \leftarrow k_{\sigma, \xi}(E, F) / \sqrt{k_{\sigma, \xi}(E, E)k_{\sigma, \xi}(F, F)}$ .

We set the rescale coefficient to  $\xi = \sigma$  and present here the heuristic method to select the bandwidth  $\sigma$ . Given the kernel values calculated from the 3-dimensional persistence diagrams  $Dg_1^{(3)}, Dg_2^{(3)}, \dots, Dg_M^{(3)}$ , we denote  $\sigma_s^2 = \text{median}\{(b_i - b_j)^2 + (d_i - d_j)^2 \mid (b_i, d_i, \tau_i), (b_j, d_j, \tau_j) \in Dg_s^{(3)}\}$  with  $s = 1, 2, \dots, M$ . We set  $\sigma$  as  $\sigma^2 = \frac{1}{2} \text{median}\{\sigma_s^2 \mid s = 1, \dots, N\}$ , such that  $2\sigma^2$  takes values close to many  $(b_i - b_j)^2 + (d_i - d_j)^2$  values.

**Common statistical measures from network.** For each network, we calculate the following 16 common measures; density (the ratio of existing to possible edges), transitivity<sup>13</sup> (the proportion of triangles), diameter (the maximum eccentricity), radius (the minimum eccentricity), degree assortativity coefficient<sup>56</sup>, global efficiency<sup>57</sup>, the number of connected parts, the average number of triangles that include a node as a vertex, average local efficiency<sup>57</sup>, average edge betweenness centrality<sup>58</sup>, average node betweenness centrality<sup>59</sup>, average node closeness centrality<sup>59</sup>, average eccentricity, average shortest paths, and average degree centrality<sup>59</sup>. We normalize the measures in range  $[0, 1]$  by Min-Max normalization (i.e.,  $f = (f - f_{\min}) / (f_{\max} - f_{\min})$  where  $f_{\min}, f_{\max}$  are the minimum and maximum values of the measure in the data).

**Real-world network data.** In the classification task, we test on ten real-world network datasets of bioinformatics and social networks<sup>50</sup>. Supplementary Table 1 shows the aggregate statistics for these datasets.

The first dataset is MUTAG<sup>60</sup>; it consists of 188 chemical compounds networks divided into two classes according to their mutagenic effect on a bacterium, i.e., mutagenic aromatic and heteroaromatic nitro compounds.

BZR, COX2, DHFR<sup>61</sup> datasets consist of 405 ligands for benzodiazepine receptor (BZR), 467 cyclooxygenase-2 inhibitors (COX2), and 756 inhibitors of dihydrofolate reductase (DHFR) come with 3D coordinates. In each of these datasets, the chemical compounds are divided into active and inactive compounds that we need to classify.

FRANKENSTEIN<sup>62</sup> is a modified version of BURSI<sup>63</sup> dataset made by 4337 molecules with 2401 mutagens and 1936 nonmutagens to classify. Each molecule is represented as a small network whose vertices are labeled by the chemical atom symbol and edges by the bond type.

PROTEINS<sup>64</sup> is a dataset of 1128 proteins represented as networks where nodes are secondary structure elements, and edge represent neighborhood within the 3-D structure or along the amino acid chain. We classify proteins into enzymes and non-enzymes.

NCI1 and NCI109<sup>65</sup> are datasets of chemical compounds with 4100 and 4127 compounds, respectively. We classify the compounds with the ability to suppress or inhibit the growth of a panel of human tumor cell lines.

IMDB-BINARY<sup>66</sup> is a dataset of 1000 movie collaboration ego-networks for each actor (actress) on Action and Romance genres from IMDB.com. For each network, two nodes representing actors or actresses are connected if they appear in the same movie. The task is to identify whether a given ego-network of an actor (actress) belongs to Action or Comedy genre.

IMDB-MULTI<sup>66</sup> is the multi-class version of IMDB-BINARY and contains 1500 ego-networks belong to Comedy, Romance and Sci-Fi genres.

**Code availability.** The C++ code for calculating persistent diagrams (with core implementation referenced from Ripser library<sup>67</sup>) and kernel, the Python code for mapping network nodes into a point cloud, the R code for calculating other kernel methods, the Matlab code for generating network benchmarks are publicly available at the GitHub repository <https://github.com/OminiaVincit/scale-variant-topo>.

**Data availability.** The data that support the findings of this study are available from the corresponding author on reasonable request. However, benchmark networks can be generated by using the source code in the “Code availability” section. For real networks data that have been obtained from publicly available sources, the corresponding URLs or references are provided in the “Real networks data”.

## References

1. Taylor, D. *et al.* Topological data analysis of contagion maps for examining spreading processes on networks. *Nat. Commun.* **6**, 7723 (2015).
2. Zañudo, J. G. T., Yang, G. & Albert, R. Structure-based control of complex networks with nonlinear dynamics. *Proc. Natl Acad. Sci. USA* **114**, 7234–7239 (2017).
3. Santolini, M. & Barabási, A.-L. Predicting perturbation patterns from the topology of biological networks. *Proc. Natl Acad. Sci. USA* **115**, E6375–E6383 (2018).
4. Sun, K., Gonçalves, J. P., Larminie, C. & Pržulj, N. Predicting disease associations via biological network analysis. *BMC Bioinformatics* **15**, 304 (2014).
5. Calderone, A. *et al.* Comparing alzheimer’s and parkinson’s diseases networks using graph communities structure. *BMC Syst. Biol.* **10**, 25 (2016).
6. Schieber, T. A. *et al.* Quantification of network structural dissimilarities. *Nat. Commun.* **8**, 13928 (2017).
7. Carpi, L., Saco, P., Rosso, O. & Ravetti, M. Structural evolution of the tropical pacific climate network. *Eur. Phys. J. B* **85**, 389 (2012).

8. Barnett, I. & Onnela, J.-P. Change point detection in correlation networks. *Sci. Rep.* **6**, 18893 (2016).
9. Bao, W. & Michailidis, G. Core community structure recovery and phase transition detection in temporally evolving networks. *Sci. Rep.* **8**, 12938 (2018).
10. Ahn, Y.-Y., Bagrow, J. P. & Lehmann, S. Link communities reveal multiscale complexity in networks. *Nature* **466**, 761 (2010).
11. Betzel, R. F. & Bassett, D. S. Multi-scale brain networks. *Neuroimage* **160**, 73–83 (2017).
12. Boulos, R. E., Tremblay, N., Arneodo, A., Borgnat, P. & Audit, B. Multi-scale structural community organisation of the human genome. *BMC Bioinformatics* **18**, 209 (2017).
13. Costa, L. d. F., Rodrigues, F. A., Traverso, G. & Villas Boas, P. R. Characterization of complex networks: A survey of measurements. *Adv. Phys.* **56**, 167–242 (2007).
14. Newman, M. E. J. *Networks: An Introduction* (Oxford Univ. Press, 2010).
15. Arenas, A., Díaz-Guilera, A. & Pérez-Vicente, C. J. Synchronization reveals topological scales in complex networks. *Phys. Rev. Lett.* **96**, 114102 (2006).
16. Sales-Pardo, M., Guimera, R., Moreira, A. A. & Amaral, L. A. N. Extracting the hierarchical organization of complex systems. *Proc. Natl Acad. Sci. USA* **104**, 15224–15229 (2007).
17. Lancichinetti, A., Fortunato, S. & Kertész, J. Detecting the overlapping and hierarchical community structure in complex networks. *New J. Phys.* **11**, 033015 (2009).
18. Tremblay, N. & Borgnat, P. Graph wavelets for multiscale community mining. *IEEE Trans. Signal Process.* **62**, 5227–5239 (2014).
19. Marvel, S. A., Kleinberg, J., Kleinberg, R. D. & Strogatz, S. H. Continuous-time model of structural balance. *Proc. Natl Acad. Sci. USA* **108**, 1771–1776 (2011).
20. van der Schaft, A., Rao, S. & Jayawardhana, B. On the mathematical structure of balanced chemical reaction networks governed by mass action kinetics. *SIAM J. Appl. Math.* **73**, 953–973 (2013).
21. Reimann, M. W. *et al.* Cliques of neurons bound into cavities provide a missing link between structure and function. *Frontiers in Computational Neuroscience* **48** (2017).
22. de Menezes, M. A. & Barabási, A.-L. Fluctuations in network dynamics. *Phys. Rev. Lett.* **92**, 028701 (2004).
23. Wells, D. K., Kath, W. L. & Motter, A. E. Control of stochastic and induced switching in biophysical networks. *Phys. Rev. X* **5**, 031036 (2015).
24. Hindes, J. & Schwartz, I. B. Epidemic extinction and control in heterogeneous networks. *Phys. Rev. Lett.* **117**, 028302 (2016).
25. Barabási, A.-L. *et al.* *Network science* (Cambridge Univ. Press, 2016).
26. Edelsbrunner, H. & Harer, J. *Computational Topology. An Introduction.* (Amer. Math. Soc., 2010).
27. Edelsbrunner, H., Letscher, D. & Zomorodian, A. Topological persistence and simplification. *Discrete Comput. Geom.* **28**, 511–533 (2002).
28. Zomorodian, A. & Carlsson, G. Computing persistent homology. *Discrete Comput. Geom.* **33**, 249–274 (2005).
29. Carlsson, G. Topology and data. *Bull. Amer. Math. Soc.* **46**, 255–308 (2009).
30. Kaczynski, T., Mischaikow, K. & Mrozek, M. *Computational homology*, vol. 157 (Springer, 2006).
31. Mischaikow, K. & Nanda, V. Morse theory for filtrations and efficient computation of persistent homology. *Discrete Comput. Geom.* **50**, 330–353 (2013).
32. Tran, Q. H. & Hasegawa, Y. Topological time-series analysis with delay-variant embedding (2018). Preprint at [arXiv:1803.00208](https://arxiv.org/abs/1803.00208).
33. Harchaoui, Z., Moulines, E. & Bach, F. R. Kernel change-point analysis. In *Adv. Neural Inf. Process. Syst.*, 609–616 (2009).
34. Chazal, F., de Silva, V. & Oudot, S. Persistence stability for geometric complexes. *Geometriae Dedicata* **173**, 193–214 (2014).

35. Golub, G. H. & Van Loan, C. F. *Matrix computations*, vol. 3 (JHU Press, 2012).
36. Newman, M. E. J. & Girvan, M. Finding and evaluating community structure in networks. *Phys. Rev. E* **69**, 026113 (2004).
37. Lancichinetti, A., Fortunato, S. & Radicchi, F. Benchmark graphs for testing community detection algorithms. *Phys. Rev. E* **78**, 046110 (2008).
38. Lancichinetti, A. & Fortunato, S. Benchmarks for testing community detection algorithms on directed and weighted graphs with overlapping communities. *Phys. Rev. E* **80**, 016118 (2009).
39. Erdős, P. & Rényi, A. On random graphs I. *Publ. Math.* **6**, 290–297 (1959).
40. Watts, D. J. & Strogatz, S. H. Collective dynamics of 'small-world' networks. *Nature* **393**, 440–442 (1998).
41. Newman, M. E., Strogatz, S. H. & Watts, D. J. Random graphs with arbitrary degree distributions and their applications. *Phys. Rev. E* **64**, 026118 (2001).
42. Bishop, C. M. *Pattern Recognition and Machine Learning (Information Science and Statistics)* (Springer, 2006).
43. Kashima, H., Tsuda, K. & Inokuchi, A. Marginalized kernels between labeled graphs. In *Proceedings of the 20th international conference on machine learning*, 321–328 (2003).
44. Gärtner, T., Flach, P. & Wrobel, S. On graph kernels: Hardness results and efficient alternatives. In *Proceedings of the 16th Annual Conference on Computational Learning Theory*, 129–143 (2003).
45. Borgwardt, K. M. & Kriegel, H.-P. Shortest-path kernels on graphs. In *Proceedings of the 5th IEEE International Conference on Data Mining*, 74–81 (2005).
46. Borgwardt, K. M., Petri, T., Vishwanathan, S. & Kriegel, H.-P. An efficient sampling scheme for comparison of large graphs. *MLG* (2007).
47. Shervashidze, N., Schweitzer, P., Leeuwen, E. J. v., Mehlhorn, K. & Borgwardt, K. M. Weisfeiler-lehman graph kernels. *JMLR* **12**, 2539–2561 (2011).
48. Sugiyama, M., Ghisu, M. E., Llinares-López, F. & Borgwardt, K. graphkernels: R and python packages for graph comparison. *Bioinformatics* **34**, 530–532 (2017).
49. De Domenico, M. Diffusion geometry unravels the emergence of functional clusters in collective phenomena. *Phys. Rev. Lett.* **118**, 168301 (2017).
50. Kersting, K., Kriege, N. M., Morris, C., Mutzel, P. & Neumann, M. Benchmark data sets for graph kernels (2016). <http://graphkernels.cs.tu-dortmund.de>.
51. Arbeitman, M. N. *et al.* Gene expression during the life cycle of drosophila melanogaster. *Science* **297**, 2270–2275 (2002).
52. Zhang, J. & Cao, J. Finding common modules in a time-varying network with application to the drosophila melanogaster gene regulation network. *J. Am. Stat. Assoc.* **112**, 994–1008 (2017).
53. Song, L., Kolar, M. & Xing, E. P. Keller: estimating time-varying interactions between genes. *Bioinformatics* **25**, i128–i136 (2009).
54. De Silva, V. & Carlsson, G. E. Topological estimation using witness complexes. *SPBG* **4**, 157–166 (2004).
55. Sheehy, D. R. Linear-size approximations to the vietoris–rips filtration. *Discrete Comput. Geom.* **49**, 778–796 (2013).
56. Newman, M. E. Assortative mixing in networks. *Phys. Rev. Lett.* **89**, 208701 (2002).
57. Latora, V. & Marchiori, M. Efficient behavior of small-world networks. *Phys. Rev. Lett.* **87**, 198701 (2001).
58. Brandes, U. On variants of shortest-path betweenness centrality and their generic computation. *Soc. Networks* **30**, 136–145 (2008).
59. Freeman, L. C. Centrality in social networks conceptual clarification. *Soc. Networks* **1**, 215–239 (1978).
60. Debnath, A. K., Lopez de Compadre, R. L., Debnath, G., Shusterman, A. J. & Hansch, C. Structure-activity relationship of mutagenic aromatic and heteroaromatic nitro compounds. correlation with molecular orbital energies and hydrophobicity. *J. Med. Chem.* **34**, 786–797 (1991).

61. Sutherland, J. J., O'brien, L. A. & Weaver, D. F. Spline-fitting with a genetic algorithm: A method for developing classification structure- activity relationships. *J. Chem. Inf. Comput. Sci.* **43**, 1906–1915 (2003).
62. Orsini, F., Frasconi, P. & De Raedt, L. Graph invariant kernels. In *Proceedings of the 24th International Joint Conference on Artificial Intelligence*, 3756–3762 (2015).
63. Kazius, J., McGuire, R. & Bursi, R. Derivation and validation of toxicophores for mutagenicity prediction. *J. Med. Chem.* **48**, 312–320 (2005).
64. Borgwardt, K. M. *et al.* Protein function prediction via graph kernels. *Bioinformatics* **21**, i47–i56 (2005).
65. Wale, N., Watson, I. A. & Karypis, G. Comparison of descriptor spaces for chemical compound retrieval and classification. *Knowledge and Information Systems* **14**, 347–375 (2008).
66. Yanardag, P. & Vishwanathan, S. Deep graph kernels. In *Proceedings of the 21th ACM SIGKDD International Conference on Knowledge Discovery and Data Mining*, 1365–1374 (2015).
67. Bauer, U. Ripser: a lean C++ code for the computation of Vietoris–Rips persistence barcodes (2017). <https://github.com/Ripser/ripser>.

# Supplemental Material for “Scale-variant Topological Information for Characterizing Complex Networks”

Quoc Hoan Tran, Van Tuan Vo and Yoshihiko Hasegawa

This supplementary material describes in detail the calculations introduced in the main text and additional figures. Equation in this section are prefixed with S (e.g., Eq. (S1)). Numbers without the prefix (e.g., Eq. (1)) refer to items in the main text.

## Supplementary Notes

### Supplementary Note 1: Construction of Vietoris–Rips filtration on a network.

In what follows, we define and describe in Supplementary Fig. 1 the process to extract the topological features of complex network at each specific time scale  $\tau$ .

We consider an undirected weighted network  $\mathcal{G}$  with  $N$  nodes  $v_1, \dots, v_N$ . We denote  $\mathbf{L}_{\mathcal{G}}^{\text{rw}}$  as the random walk Laplacian of the network  $\mathcal{G}$ . At a specific  $\tau$ , we map nodes of the network  $\mathcal{G}$  to a point cloud of  $N$  points  $\mathbf{p}_{\mathcal{G}}(\tau|1), \dots, \mathbf{p}_{\mathcal{G}}(\tau|N)$ . Here,  $\mathbf{p}_{\mathcal{G}}(\tau|i)$  is given by the solution of the Kolmogorov forward equation

$$\frac{d\mathbf{p}_{\mathcal{G}}(\tau|i)}{dt} = -\mathbf{p}_{\mathcal{G}}(\tau|i)\mathbf{L}_{\mathcal{G}}^{\text{rw}}. \quad (\text{S1})$$

The solution for Eq. S1 is  $\mathbf{p}_{\mathcal{G}}(\tau|i) = \mathbf{u}_i \exp(-\tau\mathbf{L}_{\mathcal{G}}^{\text{rw}})$ , where  $\mathbf{u}_i = [0, \dots, 0, 1, 0, \dots, 0]$  with its  $i$ -th element being equal to 1; others are equal to 0.

At each  $\tau$  we calculate the diffusion distance matrix  $\Delta_{\tau}$  of size  $N \times N$  whose element  $\Delta_{ij}$  is the Euclidean distance between points  $\mathbf{p}_{\mathcal{G}}(\tau|i)$  and  $\mathbf{p}_{\mathcal{G}}(\tau|j)$  (Supplementary Fig. 1a). If  $\varepsilon = 0$ , nodes of the network can be considered as discrete points. As we increase  $\varepsilon$ , new pairwise connections and simplices may appear when  $\varepsilon$  meets each value of  $\Delta_{ij}$ . We obtain a filtration as a sequence of embedded simplicial complexes. The hole patterns such as connected components or loops can appear or disappear over this filtration. For instance, in Supplementary Fig. 1b, at  $\varepsilon = 0.025$  we have six separated nodes considered as six separated connected components, but at  $\varepsilon = 0.407$  three nodes are connected with each other; thus two connected components disappear at this scale. We can describe these patterns as two blue bars started at scale 0 and ended at scale 0.407. The same explanation with the red bar started at scale 0.428 and ended at scale 0.430, which represents the emergence of loop pattern ( $v_1 \rightarrow v_2 \rightarrow v_3 \rightarrow v_5 \rightarrow v_1$ ) at  $\varepsilon = 0.428$  and the vanishment at  $\varepsilon = 0.430$ . Supplementary Figure 1c illustrates the corresponding persistence diagrams for 0-dimensional holes and 1-dimensional holes where the birth-scale and death-scale represent for the values of  $\varepsilon$  at the emergence and vanishment of holes.

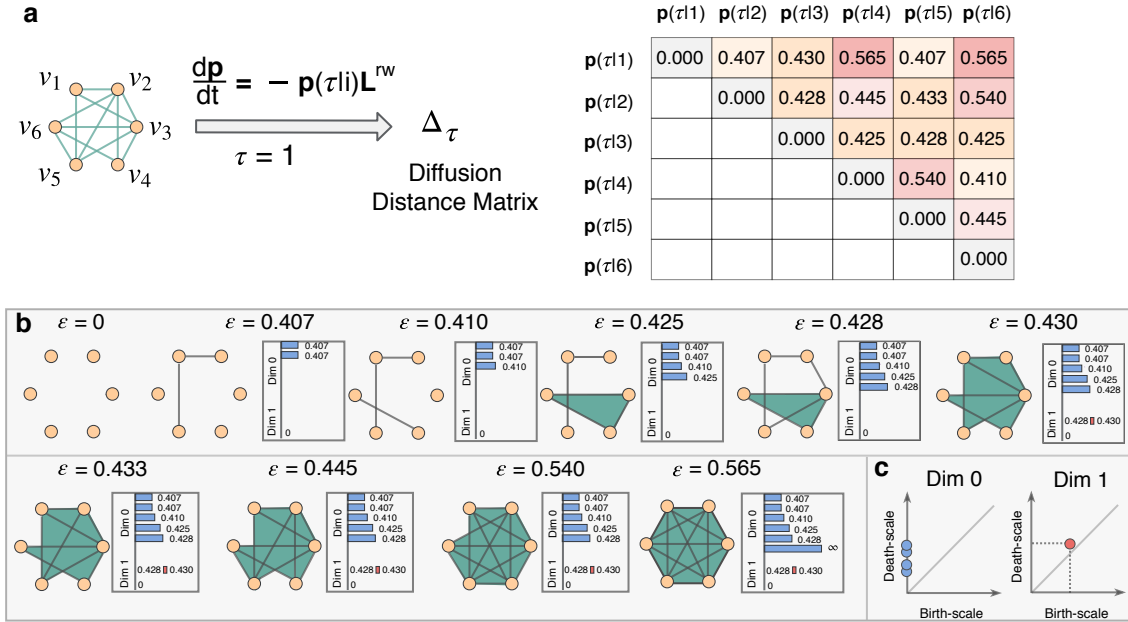
### Supplementary Note 2: Stability of scale-variant topological features

To prove the stability property of topological features undergo network perturbation, first, we introduce the concept of bottleneck distance between two 2-dimensional diagrams. Let  $X$  and  $Y$  be finite sets of points embedded in the Euclidean space  $\mathbb{R}^n$ . Denote their 2-dimensional persistent diagrams for  $l$ -dimensional holes as  $DgX$  and  $DgY$ , respectively. We consider all matchings  $\gamma$  such that a point on a diagram is matched to a point on the other or to its projection on the line  $b = d$  in 2-dimensional space. The bottleneck distance  $d_B^{(2)}$  between  $DgX$  and  $DgY$  is defined as the infimum of the longest matched infinity-norm distance over all matchings,  $\gamma$ :

$$d_B^{(2)}(DgX, DgY) = \inf_{\gamma} \max_{(\mathbf{p}, \mathbf{q}) \in \gamma} \|\mathbf{p} - \mathbf{q}\|_{\infty}. \quad (\text{S2})$$

The bottleneck distance between the 2-dimensional persistence diagrams satisfies the following inequality<sup>1</sup>:

$$d_B^{(2)}(DgX, DgY) \leq 2d_H(X, Y), \quad (\text{S3})$$



**Supplementary Figure 1 | Construction of Vietoris–Rips filtration of complex network at a specific time scale  $\tau$ .** We map nodes  $v_1, \dots, v_N$  of the network to a point cloud of  $N$  points  $\mathbf{p}(\tau|1), \dots, \mathbf{p}(\tau|N)$  through a diffusion dynamics described by random walk Laplacian  $\mathbf{L}^{\text{rw}}$ . **(a)** Diffusion distance matrix  $\Delta_\tau$  of size  $N \times N$  whose element  $\Delta_{ij}$  is the Euclidean distance between points  $\mathbf{p}(\tau|i)$  and  $\mathbf{p}(\tau|j)$ . **(b)** A complex is built over a set of points if the pairwise distances between them are less than or equal to a distance-scale parameter  $\varepsilon$ . If  $\varepsilon = 0$  we have the discrete points. As  $\varepsilon$  takes the increasing sequence values of diffusion distance  $\Delta_{ij}$ , hole patterns such as connected components (0-dimensional hole) or loops (1-dimensional hole) can appear or disappear over this filtration. The life-time of these hole patterns are described as blue bars (for 0-dimensional holes) and red bars (for 1-dimensional holes). These bars begin at values of  $\varepsilon$  when the holes appear, then end at values when the holes disappear. **(c)** The corresponding persistence diagrams for 0-dimensional holes and 1-dimensional holes. The birth-scale and death-scale represent for the values of  $\varepsilon$  at the emergence and vanishment of the holes.

where  $d_H(X, Y)$  is the Hausdorff distance given by

$$d_H(X, Y) = \max \left\{ \max_{\mathbf{x} \in X} \min_{\mathbf{y} \in Y} d(\mathbf{x}, \mathbf{y}), \max_{\mathbf{y} \in Y} \min_{\mathbf{x} \in X} d(\mathbf{x}, \mathbf{y}) \right\}. \quad (\text{S4})$$

Here,  $d(\mathbf{x}, \mathbf{y})$  is the Euclidean distance between two points  $\mathbf{x}, \mathbf{y}$  in  $\mathbb{R}^n$ .

Given two 3-dimensional persistence diagrams as  $E$  and  $F$ , consider all matchings  $\psi$  such that a point on a diagram is matched to a point on the other or to its projection on the plane  $b = d$ . For each pair  $(\mathbf{p}, \mathbf{q}) \in \psi$  for which  $\mathbf{p} = (b_1, d_1, \tau_1)$  and  $\mathbf{q} = (b_2, d_2, \tau_2)$ , we define the *relative infinity-norm distance* between  $\mathbf{p}$  and  $\mathbf{q}$  as  $d_\xi^{(\infty)}(\mathbf{p}, \mathbf{q}) = \max(|b_1 - b_2|, |d_1 - d_2|, \xi|\tau_1 - \tau_2|)$ , where  $\xi$  is a positive rescaling coefficient introduced to adjust the scale difference between the point-wise distance and time. The bottleneck distance,  $d_{B, \xi}^{(3)}(E, F)$ , is defined as the infimum of the longest matched relative infinity-norm distance over all matchings,  $\psi$ :

$$d_{B, \xi}^{(3)}(E, F) = \inf_{\psi} \max_{(\mathbf{p}, \mathbf{q}) \in \psi} d_\xi^{(\infty)}(\mathbf{p}, \mathbf{q}). \quad (\text{S5})$$

For each  $\tau \in \mathcal{T}$  and  $\mathcal{G}, \mathcal{H}$  are two networks with the same number  $N$  of nodes, first, we prove the following inequality:

$$d_B^{(2)}(Dg_{l, \tau}^{(2)}(\mathcal{G}), Dg_{l, \tau}^{(2)}(\mathcal{H})) \leq 2\tau \|\mathbf{L}_{\mathcal{G}}^{\text{rw}} - \mathbf{L}_{\mathcal{H}}^{\text{rw}}\|_2. \quad (\text{S6})$$

Here, two 2-dimensional persistence diagrams  $Dg_{l, \tau}^{(2)}(\mathcal{G})$  and  $Dg_{l, \tau}^{(2)}(\mathcal{H})$  are calculated for  $l$ -dimensional holes from two point clouds  $\mathbf{P}_{\mathcal{G}, \tau} = \{\mathbf{p}_{\mathcal{G}}(\tau|1), \dots, \mathbf{p}_{\mathcal{G}}(\tau|N)\}$  and  $\mathbf{P}_{\mathcal{H}, \tau} = \{\mathbf{p}_{\mathcal{H}}(\tau|1), \dots, \mathbf{p}_{\mathcal{H}}(\tau|N)\}$ , respectively.

Apply Eq. S3 with  $\mathbf{P}_{\mathcal{G}, \tau}$  and  $\mathbf{P}_{\mathcal{H}, \tau}$ , we have

$$d_B^{(2)}(Dg_{l, \tau}^{(2)}(\mathcal{G}), Dg_{l, \tau}^{(2)}(\mathcal{H})) \leq 2d_H(\mathbf{P}_{\mathcal{G}, \tau}, \mathbf{P}_{\mathcal{H}, \tau}), \quad (\text{S7})$$

From the definition of Hausdorff distance, we have

$$d_H(\mathbf{P}_{\mathcal{G}, \tau}, \mathbf{P}_{\mathcal{H}, \tau}) = \max \left\{ \max_i \min_j d(\mathbf{p}_{\mathcal{G}}(\tau|i), \mathbf{p}_{\mathcal{H}}(\tau|j)), \max_j \min_i d(\mathbf{p}_{\mathcal{G}}(\tau|i), \mathbf{p}_{\mathcal{H}}(\tau|j)) \right\} \quad (\text{S8})$$

$$\leq \max \left\{ \max_i d(\mathbf{p}_{\mathcal{G}}(\tau|i), \mathbf{p}_{\mathcal{H}}(\tau|i)), \max_j d(\mathbf{p}_{\mathcal{G}}(\tau|j), \mathbf{p}_{\mathcal{H}}(\tau|j)) \right\} \quad (\text{S9})$$

$$\leq \max_i d(\mathbf{p}_{\mathcal{G}}(\tau|i), \mathbf{p}_{\mathcal{H}}(\tau|i)). \quad (\text{S10})$$

Because  $\mathbf{p}_{\mathcal{G}}(\tau|i) = \mathbf{u}_i \exp(-\tau \mathbf{L}_{\mathcal{G}}^{\text{rw}})$  and  $\mathbf{p}_{\mathcal{H}}(\tau|i) = \mathbf{u}_i \exp(-\tau \mathbf{L}_{\mathcal{H}}^{\text{rw}})$ , we have

$$d(\mathbf{p}_{\mathcal{G}}(\tau|i), \mathbf{p}_{\mathcal{H}}(\tau|i)) = \|\mathbf{u}_i (e^{-\tau \mathbf{L}_{\mathcal{G}}^{\text{rw}}} - e^{-\tau \mathbf{L}_{\mathcal{H}}^{\text{rw}}})\|_2 \quad (\text{S11})$$

$$\leq \|\mathbf{u}_i\|_2 \|e^{-\tau \mathbf{L}_{\mathcal{G}}^{\text{rw}}} - e^{-\tau \mathbf{L}_{\mathcal{H}}^{\text{rw}}}\|_2 = \|e^{-\tau \mathbf{L}_{\mathcal{G}}^{\text{rw}}} - e^{-\tau \mathbf{L}_{\mathcal{H}}^{\text{rw}}}\|_2. \quad (\text{S12})$$

We write the difference of matrix exponential in terms of an integral<sup>2</sup>,

$$\|e^{-\tau \mathbf{L}_{\mathcal{G}}^{\text{rw}}} - e^{-\tau \mathbf{L}_{\mathcal{H}}^{\text{rw}}}\|_2 = \left\| \int_0^\tau e^{-\mathbf{L}_{\mathcal{G}}^{\text{rw}}(\tau-t)} \mathbf{E} e^{-\mathbf{L}_{\mathcal{H}}^{\text{rw}}t} dt \right\|_2 \quad (\text{S13})$$

$$\leq \int_0^\tau \|e^{-\mathbf{L}_{\mathcal{G}}^{\text{rw}}(\tau-t)} \mathbf{E} e^{-\mathbf{L}_{\mathcal{H}}^{\text{rw}}t}\|_2 dt \leq \|\mathbf{E}\|_2 \int_0^\tau \|e^{-\mathbf{L}_{\mathcal{G}}^{\text{rw}}(\tau-t)}\|_2 \|e^{-\mathbf{L}_{\mathcal{H}}^{\text{rw}}t}\|_2 dt, \quad (\text{S14})$$

where  $\mathbf{E} = \mathbf{L}_{\mathcal{G}}^{\text{rw}} - \mathbf{L}_{\mathcal{H}}^{\text{rw}}$ . We know that  $-\mathbf{L}_{\mathcal{G}}^{\text{rw}}$  is a negative semi-definite matrix with largest eigenvalue is equal to 0. It implies that the largest eigenvalue of  $e^{-\mathbf{L}_{\mathcal{G}}^{\text{rw}}(\tau-t)}$  is equal to 1, and hence  $\|e^{-\mathbf{L}_{\mathcal{G}}^{\text{rw}}(\tau-t)}\|_2 = 1$ . We obtain the same result with  $-\mathbf{L}_{\mathcal{H}}^{\text{rw}}$ , i.e.,  $\|e^{-\mathbf{L}_{\mathcal{H}}^{\text{rw}}t}\|_2 = 1$ . Then, from Eq. (S12) and Eq. (S14), we have

$$d(\mathbf{p}_{\mathcal{G}}(\tau|i), \mathbf{p}_{\mathcal{H}}(\tau|i)) \leq \|\mathbf{E}\|_2 \int_0^\tau 1 dt = \tau \|\mathbf{E}\|_2 = \tau \|\mathbf{L}_{\mathcal{G}}^{\text{rw}} - \mathbf{L}_{\mathcal{H}}^{\text{rw}}\|_2. \quad (\text{S15})$$

From Eq. (S7), Eq. (S10) and Eq. (S15) we have the result in Eq. (S6).

Let  $\Gamma_\tau$  be the set of matchings defined in Eq. (S2) between two 2-dimensional persistence diagrams  $Dg_{l, \tau}^{(2)}(\mathcal{G})$  and  $Dg_{l, \tau}^{(2)}(\mathcal{H})$ . For each collection  $\Lambda = \{\gamma_1, \gamma_2, \dots, \gamma_K \mid \gamma_i \in \Gamma_\tau, i = 1, 2, \dots, K\}$ , we construct a matching  $\psi$  between two 3-dimensional persistence diagrams  $Dg_l^{(3)}(\mathcal{G})$  and  $Dg_l^{(3)}(\mathcal{H})$ , such that, for each  $(\mathbf{p}, \mathbf{q}) \in \psi$ , then  $\mathbf{p} = (b_1, d_1, \tau)$ ,  $\mathbf{q} = (b_2, d_2, \tau)$ , and  $(\mathbf{p}_\gamma, \mathbf{q}_\gamma) \in \gamma$ , where  $\mathbf{p}_\gamma = (b_1, d_1)$ ,  $\mathbf{q}_\gamma = (b_2, d_2)$ , and  $\gamma \in \Lambda \cap \Gamma_\tau$ . Let  $\Gamma$  be the set of all matchings  $\psi$  constructed this way. From the definition of bottleneck distance, we have the following inequality:

$$d_{B,\xi}^{(3)}(Dg_l^{(3)}(\mathcal{G}), Dg_l^{(3)}(\mathcal{H})) \leq \inf_{\psi \in \Gamma} \max_{(\mathbf{p}, \mathbf{q}) \in \psi} d_{\xi}^{(\infty)}(\mathbf{p}, \mathbf{q}). \quad (\text{S16})$$

For  $(\mathbf{p}, \mathbf{q}) \in \psi$ , we have

$$d_{\xi}^{(\infty)}(\mathbf{p}, \mathbf{q}) = \max\{|b_1 - b_2|, |d_1 - d_2|, \xi|\tau - \tau|\} \quad (\text{S17})$$

$$= \max\{|b_1 - b_2|, |d_1 - d_2|\} = \|\mathbf{p}_{\gamma} - \mathbf{q}_{\gamma}\|_{\infty}, \quad (\text{S18})$$

and Eq. (S16) becomes

$$d_{B,\xi}^{(3)}(Dg_l^{(3)}(\mathcal{G}), Dg_l^{(3)}(\mathcal{H})) \leq \max_{\tau \in \mathcal{T}} \inf_{\gamma \in \Gamma_{\tau}} \max_{(\mathbf{p}_{\gamma}, \mathbf{q}_{\gamma}) \in \gamma} \|\mathbf{p}_{\gamma} - \mathbf{q}_{\gamma}\|_{\infty} \quad (\text{S19})$$

$$= \max_{\tau \in \mathcal{T}} d_B^{(2)}(Dg_{l,\tau}^{(2)}(\mathcal{G}), Dg_{l,\tau}^{(2)}(\mathcal{H})). \quad (\text{S20})$$

From Eq. (S6) and Eq. (S20) we obtain Eq. (3) in the main text which is the stability property of our scale-variant features.

### Supplementary Note 3: Kernel Fisher discriminant ratio.

The kernel method maps persistence diagrams in an abstract space, namely a reproducing Hilbert space  $\mathcal{H}$  associated with a reproducing kernel  $k(\cdot, \cdot)$  and a feature map  $\Phi(DgX) = k(DgX, \cdot)$ . The inner product between two operators  $\Phi(DgX)$  and  $\Phi(DgY)$  is defined as  $\langle \Phi(DgX), \Phi(DgY) \rangle_{\mathcal{H}} = k(DgX, DgY)$ . Here,  $DgX$  and  $DgY$  are two 3-dimensional persistence diagrams. We consider a window as a collection of diagrams  $\mathcal{D} = \{Dg_1, \dots, Dg_M\}$  and a given index  $s > 1$ . The corresponding empirical mean elements and covariance operators associated to the data in  $\mathcal{D}$  having index before and from  $s$  are defined as

$$\hat{\mu}_1 = \frac{1}{s-1} \sum_{i=1}^{s-1} k(Dg_i, \cdot), \quad (\text{S21})$$

$$\hat{\Sigma}_1 = \frac{1}{s-1} \sum_{i=1}^{s-1} \{k(Dg_i, \cdot) - \hat{\mu}_1\} \otimes \{k(Dg_i, \cdot) - \hat{\mu}_1\}, \quad (\text{S22})$$

$$\hat{\mu}_2 = \frac{1}{M-s+1} \sum_{i=s}^M k(Dg_i, \cdot), \quad (\text{S23})$$

$$\hat{\Sigma}_2 = \frac{1}{M-s+1} \sum_{i=s}^M \{k(Dg_i, \cdot) - \hat{\mu}_2\} \otimes \{k(Dg_i, \cdot) - \hat{\mu}_2\}. \quad (\text{S24})$$

Here,  $f \otimes g$  for two operators  $f, g \in \mathcal{H}$  is defined for all operators  $h \in \mathcal{H}$  as  $(f \otimes g)h = \langle g, h \rangle_{\mathcal{H}} f$ .

The kernel Fisher discriminant ratio  $\text{KFDR}_{M,s}(\mathcal{D})$ <sup>3</sup> is defined as

$$\text{KFDR}_{M,s}(\mathcal{D}) = \frac{(s-1)(M-s+1)}{M} \left\langle \hat{\mu}_2 - \hat{\mu}_1, (\hat{\Sigma} + \gamma \mathbf{I})^{-1} (\hat{\mu}_2 - \hat{\mu}_1) \right\rangle_{\mathcal{H}}, \quad (\text{S25})$$

where  $\gamma$  is a regularization parameter and  $\hat{\Sigma} = \frac{s-1}{M} \hat{\Sigma}_1 + \frac{M-s+1}{M} \hat{\Sigma}_2$ .

We set  $\gamma = 10^{-1}, 10^{-1}, 10^{-5}$  in experiments of Girvan–Newman (GN) network, Lancichinetti–Fortunato–Radicchi (LFR) network, and *Drosophila Melanogaster* network, respectively.

### Supplementary Note 4: Graph kernel methods.

We describe graph kernel methods used in the main text. These graph kernels are based on random walks (KStepRW, GeometricRW, ExponentialRW)<sup>4,5</sup>, paths (ShortestPath<sup>6</sup>), limited-sized subgraphs (Graphlet<sup>7</sup>), and subtree patterns (Weisfeiler–Lehman<sup>8</sup>). The implementations of these graph kernels can be found in ref.<sup>9</sup>.

**Graphlet kernel.** A size- $k$  graphlet is an induced and non-isomorphic sub-graph of size  $k$ . Let  $\mathcal{S}_k = \{G_1, \dots, G_{N_k}\}$  be the set of size- $k$  graphlets where  $N_k$  denotes the number of unique graphlets of size  $k$ . For an unlabeled graph  $\mathcal{G}$ , we define a vector  $\mathbf{f}_{\mathcal{G}}$  of length  $N_k$  such that the  $i^{\text{th}}$  component of  $\mathbf{f}_{\mathcal{G}}$  denotes the frequency of graphlet  $G_i$  appearing as a subgraph of  $\mathcal{G}$ . Given two unlabeled graphs  $\mathcal{G}$  and  $\mathcal{G}'$ , the graphlet kernel is defined as

$$\mathcal{K}_{\text{GK}}(\mathcal{G}, \mathcal{G}') = \langle \mathbf{f}_{\mathcal{G}}, \mathbf{f}_{\mathcal{G}'} \rangle, \quad (\text{S26})$$

where  $\langle \cdot, \cdot \rangle$  represents for the Euclidean dot product. In our experiments, we set  $k = 4$  for MUTAG, BZR, DHFR, and FRANKENSTEIN datasets and  $k = 3$  for other datasets.

**KStepRW kernel.** To measure the similarity between two graphs, random walk graph kernel computes the number of equal-length walks in two graphs. Given two unlabeled graphs  $\mathcal{G}$  and  $\mathcal{G}'$  with their vertex and edge sets as  $(\mathcal{V}, \mathcal{E})$  and  $(\mathcal{V}', \mathcal{E}')$ , respectively. The direct product graph  $\mathcal{G}_\times = (\mathcal{V}_\times, \mathcal{E}_\times)$  of  $\mathcal{G}$  and  $\mathcal{G}'$  is a graph with the node set  $\mathcal{V}_\times = \{(v, v') \mid v \in \mathcal{V}, v' \in \mathcal{V}'\}$ , and the edge set  $\mathcal{E}_\times = \{((v_a, v'_a), (v_b, v'_b)) \mid (v_a, v_b) \in \mathcal{E}, (v'_a, v'_b) \in \mathcal{E}'\}$ . The KStepRW kernel is the  $k$ -step random walk kernel  $\mathcal{K}_\times^k$  defined by

$$\mathcal{K}_\times^k(\mathcal{G}, \mathcal{G}') = \sum_{i,j=1}^{|\mathcal{V}_\times|} \sum_{m=0}^k [\lambda_m \mathbf{W}_\times^m]_{ij}, \quad (\text{S27})$$

where  $\mathbf{W}_\times$  is a weight matrix of  $\mathcal{G}_\times$ , and a sequence of positive, real-valued weights  $\lambda_0, \dots, \lambda_k$ . In our experiments, we set  $k = 2$  and  $\lambda_0 = \lambda_1 = \lambda_2 = 1.0$ .

**GeometricRW kernel.** This kernel is the limitation of  $k$ -step random walk kernel when  $k$  goes to infinity, and the weights are the geometric series, i.e.,  $\lambda_m = \lambda^m$  ( $\lambda = 0.05$  in our experiments). GeometricRW kernel is defined as

$$\mathcal{K}_{\text{GR}}(\mathcal{G}, \mathcal{G}') = \sum_{i,j=1}^{|\mathcal{V}_\times|} \sum_{m=0}^{\infty} [\lambda^m \mathbf{W}_\times^m]_{ij} = \sum_{i,j=1}^{|\mathcal{V}_\times|} [(\mathbf{I} - \lambda \mathbf{W}_\times)^{-1}]_{ij}, \quad (\text{S28})$$

where  $\mathbf{I}$  is an identity matrix of size  $|\mathcal{V}_\times| \times |\mathcal{V}_\times|$ .

**ExponentialRW kernel.** This kernel is the limitation of  $k$ -step random walk kernel when  $k$  goes to infinity, the weights are the exponential series, i.e.,  $\lambda_m = \frac{\beta^m}{m!}$  ( $\beta = 0.1$  in our experiments). ExponentialRW kernel is defined as

$$\mathcal{K}_{\text{ER}}(\mathcal{G}, \mathcal{G}') = \sum_{i,j=1}^{|\mathcal{V}_\times|} \sum_{m=0}^{\infty} \left[ \frac{(\beta \mathbf{W}_\times)^m}{m!} \right]_{ij} = \sum_{i,j=1}^{|\mathcal{V}_\times|} [e^{\beta \mathbf{W}_\times}]_{ij}. \quad (\text{S29})$$

**ShortestPath kernel.** This kernel compares all pairs of shortest path lengths from  $\mathcal{G}$  and  $\mathcal{G}'$ , defined as

$$\mathcal{K}_{\text{SP}}(\mathcal{G}, \mathcal{G}') = \sum_{v_i, v_j \in \mathcal{G}} \sum_{v'_k, v'_l \in \mathcal{G}'} \delta(d(v_i, v_j), d(v'_k, v'_l)), \quad (\text{S30})$$

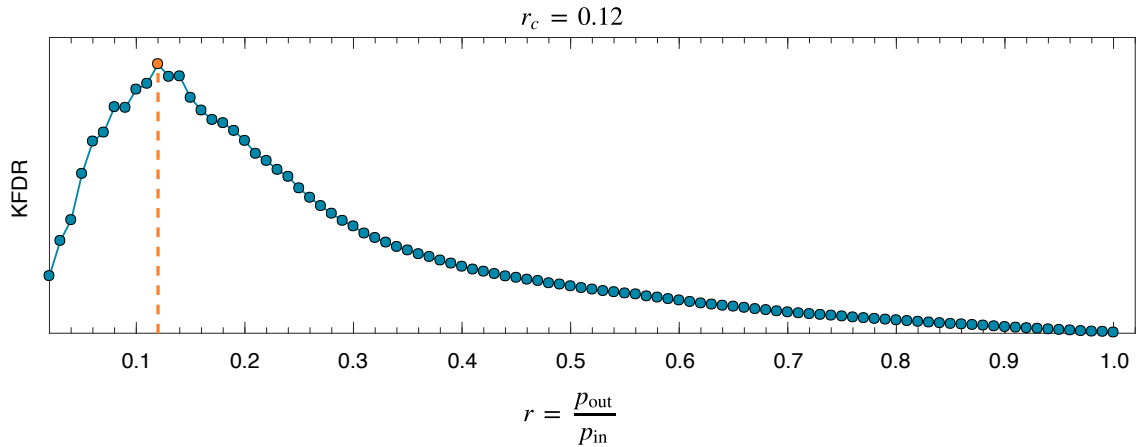
where  $d(v_i, v_j)$  and  $d(v'_k, v'_l)$  are the lengths of the shortest path between node  $v_i$  and  $v_j$  in  $\mathcal{G}$ , and the shortest path between node  $v'_k$  and  $v'_l$  in  $\mathcal{G}'$ , respectively. Here, the  $\delta$ -function is defined as  $\delta(x, y) = 1$  if  $x = y$ , and 0 if  $x \neq y$ .

**Weisfeiler–Lehman kernel.** This kernel decomposes a graph into its subtree patterns and compares these patterns in two graphs. For an unlabeled graph  $\mathcal{G}$ , all vertexes  $v$  of  $\mathcal{G}$  are initialized with label  $\phi(v) = 0$ . We iterate over each vertex  $v$  and its neighbor in order to create a multiset label as  $\phi^{(i)}(v)$  such that  $\phi^{(1)}(v) = \phi(v)$ , and  $\phi^{(i)}$  with  $i > 1$  is defined as  $\phi^{(i)}(v) = (\phi^{(i-1)}(v), \mathbf{Q}_v^{(i-1)})$  where  $\mathbf{Q}_v^{(i-1)}$  is the sorted labels of  $v$ 's neighbors. To measure the similarity between graphs, we count the co-occurrences of labels in both graphs until  $h$ -iterations with the kernel defined as

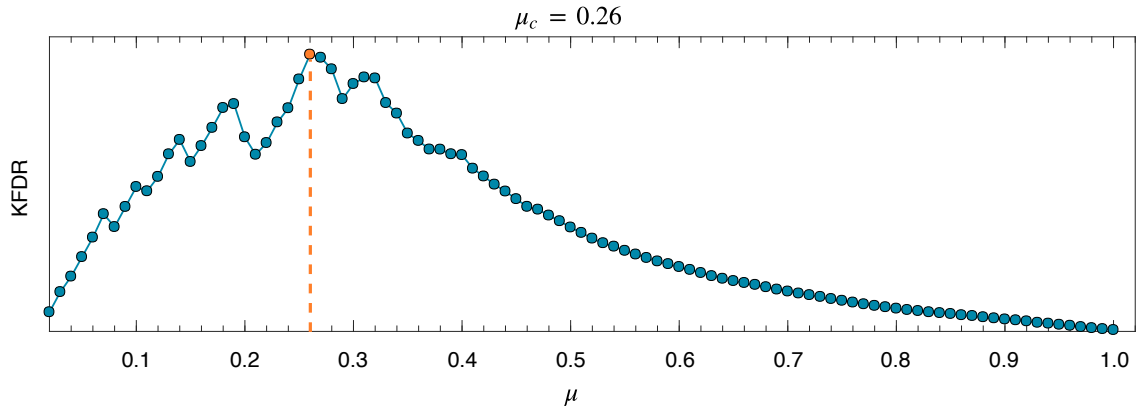
$$\mathcal{K}_{\text{WL}}(\mathcal{G}, \mathcal{G}') = \langle \mathbf{1}_{\mathcal{G}}, \mathbf{1}_{\mathcal{G}'} \rangle. \quad (\text{S31})$$

Here,  $\mathbf{1}_{\mathcal{G}}$  is the vector concatenation of  $h$  vertex label histograms  $\mathbf{1}_{\mathcal{G}}^{(1)}, \dots, \mathbf{1}_{\mathcal{G}}^{(h)}$  in  $h$  iterations. We set  $h = 5$  in our experiments.

## Supplementary Figures and Tables



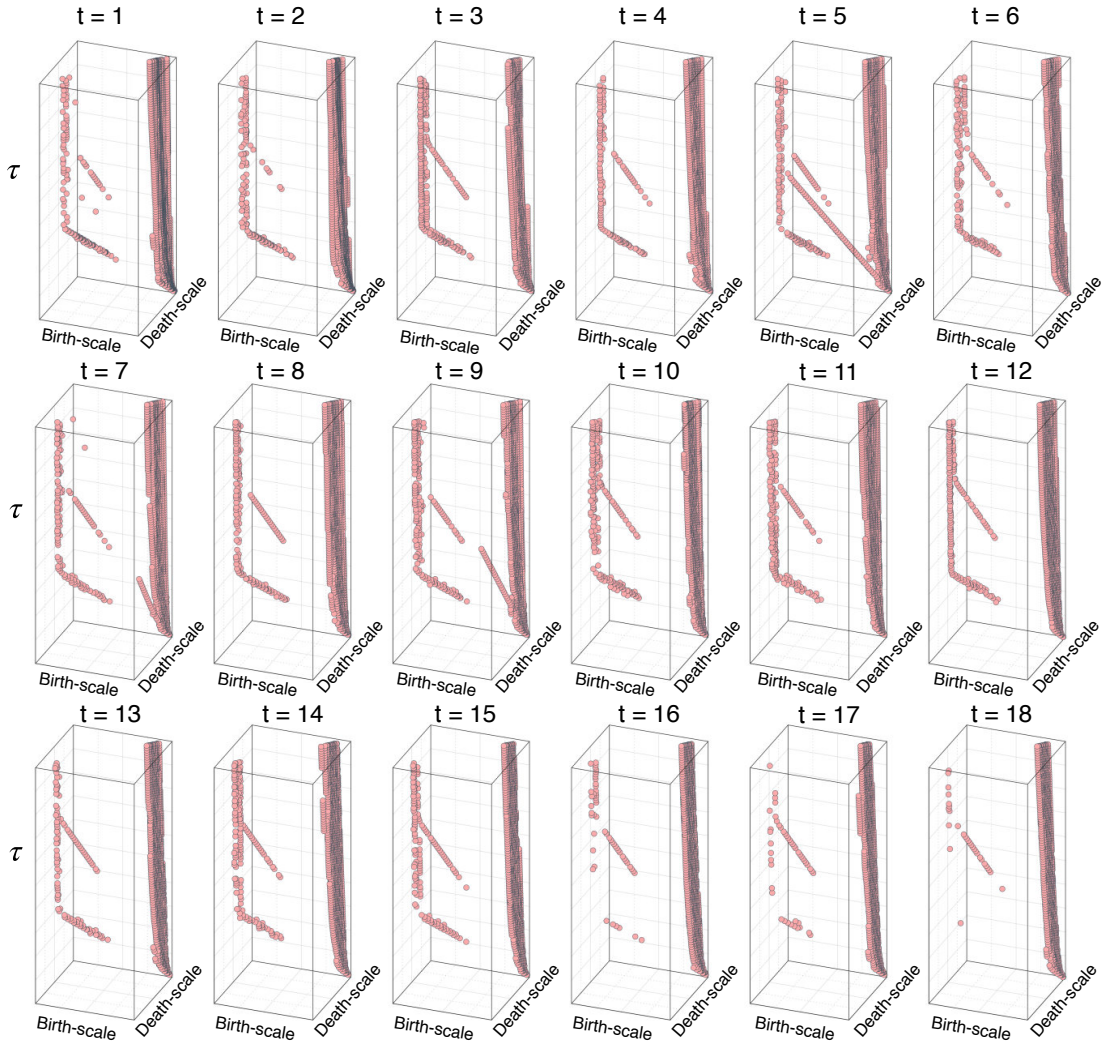
**Supplementary Figure 2 | Kernel Fisher discriminant ratio (KFDR) estimated for the series of Girvan–Newman networks.** We detect the transition point in the window of 100 persistence diagrams for 1-dimensional holes obtained when increasing  $r = p_{\text{out}}/p_{\text{in}}$  as  $r_1 = 0.01, r_2 = 0.02, \dots, r_{100} = 1.0$ . The maximum value of KFDR is marked with orange point. The transition point  $r_c = 0.12$  is the value of  $r$  that achieving maximum KFDR.



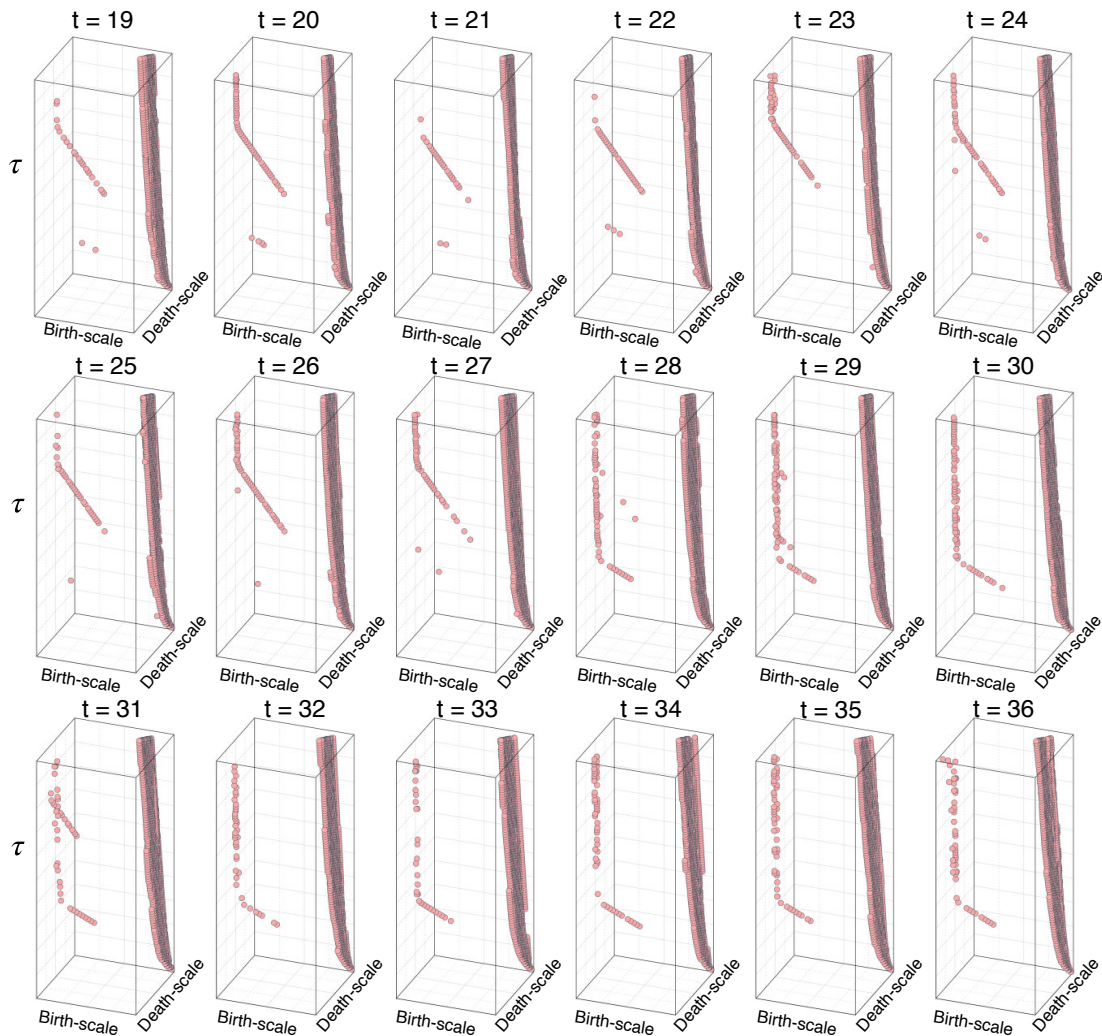
**Supplementary Figure 3 | Kernel Fisher discriminant ratio (KFDR) estimated for the series of Lancichinetti–Fortunato–Radicchi networks.** We detect the transition point in the window of 100 persistence diagrams for 1-dimensional holes obtained when increasing  $\mu$  as  $\mu_1 = 0.01, \mu_2 = 0.02, \dots, \mu_{100} = 1.0$ . The maximum value of KFDR is marked with orange point. The transition point  $\mu_c = 0.26$  is the value of  $\mu$  that achieving maximum KFDR.

**Supplementary Table 1 | Summary statistics of the real-world network data.**

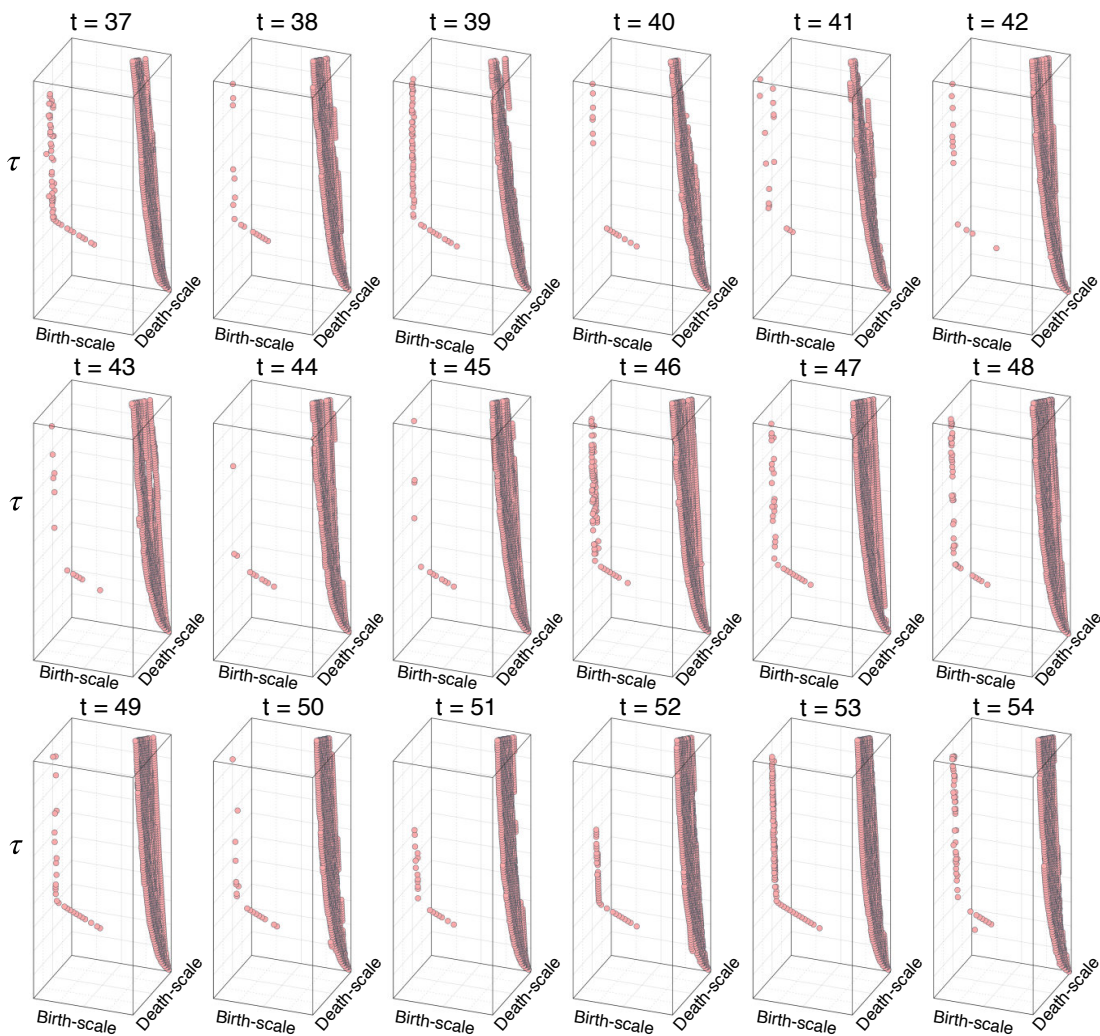
Dataset	Number of networks	Number of classes	Number of networks in each class	Average number of nodes	Average number of edges
MUTAG	188	2	(63,125)	17.93	19.79
BZR	405	2	(319, 86)	35.75	38.36
COX2	467	2	(365, 102)	41.22	43.45
DHFR	756	2	(295, 461)	42.43	44.54
FRANKENSTEIN	4337	2	(2401, 1936)	16.90	17.88
PROTEINS	1113	2	(663, 450)	39.06	72.82
NCI1	4110	2	(2053, 2057)	29.87	32.30
NCI109	4127	2	(2048, 2079)	29.68	32.13
IMDB–BINARY	1000	2	(500, 500)	19.77	96.53
IMDB–MULTI	1500	3	(500, 500, 500)	13.00	65.94



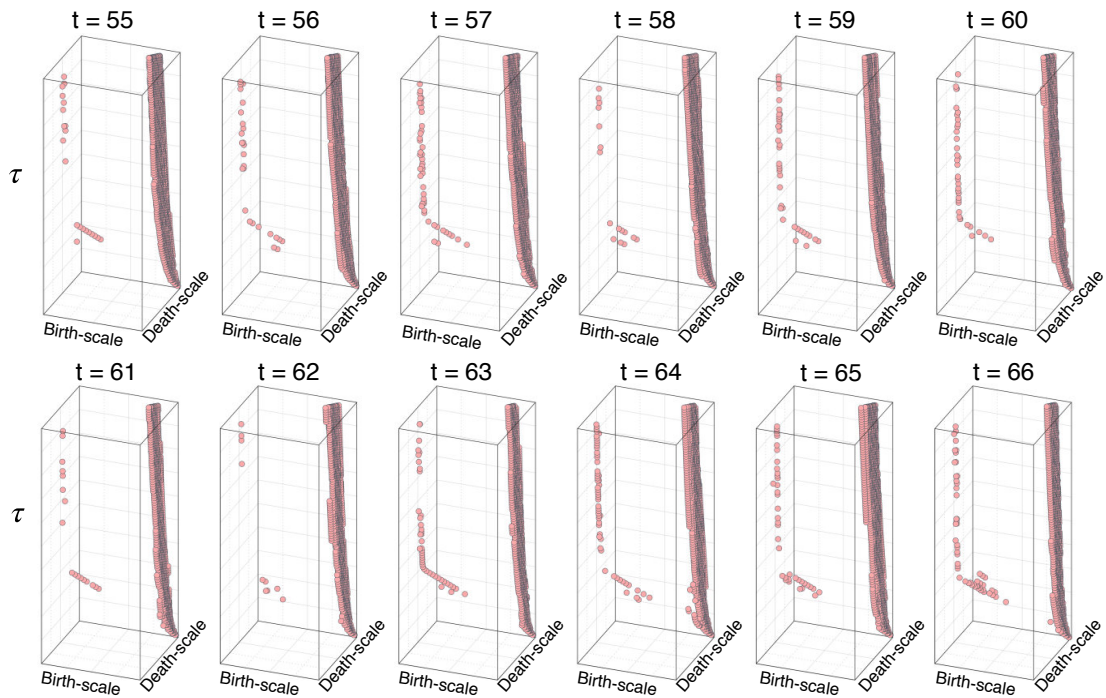
**Supplementary Figure 4 | 3-dimensional persistence diagrams of 1-dimensional holes for *Drosophila Melanogaster* gene regulatory networks spanning from  $t = 1$  to  $t = 18$ .** For each network at each time point, we compute 3-dimensional persistence diagrams with time-scale values  $\tau_1 = 1, \tau_2 = 2, \dots, \tau_{100} = 100$ . The birth-scale and death-scale axes of diagrams are represented at the logarithmic scale.



**Supplementary Figure 5 | 3-dimensional persistence diagrams of 1-dimensional holes for *Drosophila Melanogaster* gene regulatory networks spanning from  $t = 19$  to  $t = 36$ .** For each network at each time point, we compute 3-dimensional persistence diagrams with time-scale values  $\tau_1 = 1, \tau_2 = 2, \dots, \tau_{100} = 100$ . The birth-scale and death-scale axes of diagrams are represented at the logarithmic scale.



**Supplementary Figure 6 | 3-dimensional persistence diagrams of 1-dimensional holes for *Drosophila Melanogaster* gene regulatory networks spanning from  $t = 37$  to  $t = 54$ .** For each network at each time point, we compute 3-dimensional persistence diagrams with time-scale values  $\tau_1 = 1, \tau_2 = 2, \dots, \tau_{100} = 100$ . The birth-scale and death-scale axes of diagrams are represented at the logarithmic scale.



**Supplementary Figure 7 | 3-dimensional persistence diagrams of 1-dimensional holes for *Drosophila Melanogaster* gene regulatory networks spanning from  $t = 55$  to  $t = 66$ .** For each network at each time point, we compute 3-dimensional persistence diagrams with time-scale values  $\tau_1 = 1, \tau_2 = 2, \dots, \tau_{100} = 100$ . The birth-scale and death-scale axes of diagrams are represented at the logarithmic scale.

## References

1. Chazal, F., de Silva, V. & Oudot, S. Persistence stability for geometric complexes. *Geometriae Dedicata* **173**, 193–214 (2014).
2. Golub, G. H. & Van Loan, C. F. *Matrix computations*, vol. 3 (JHU Press, 2012).
3. Harchaoui, Z., Moulines, E. & Bach, F. R. Kernel change-point analysis. In *Adv. Neural Inf. Process. Syst.*, 609–616 (2009).
4. Kashima, H., Tsuda, K. & Inokuchi, A. Marginalized kernels between labeled graphs. In *Proceedings of the 20th international conference on machine learning*, 321–328 (2003).
5. Gärtner, T., Flach, P. & Wrobel, S. On graph kernels: Hardness results and efficient alternatives. In *Proceedings of the 16th Annual Conference on Computational Learning Theory*, 129–143 (2003).
6. Borgwardt, K. M. & Kriegel, H.-P. Shortest-path kernels on graphs. In *Proceedings of the 5th IEEE International Conference on Data Mining*, 74–81 (2005).
7. Borgwardt, K. M., Petri, T., Vishwanathan, S. & Kriegel, H.-P. An efficient sampling scheme for comparison of large graphs. *MLG* (2007).
8. Shervashidze, N., Schweitzer, P., Leeuwen, E. J. v., Mehlhorn, K. & Borgwardt, K. M. Weisfeiler-lehman graph kernels. *JMLR* **12**, 2539–2561 (2011).
9. Sugiyama, M., Ghisu, M. E., Llinares-López, F. & Borgwardt, K. graphkernels: R and python packages for graph comparison. *Bioinformatics* **34**, 530–532 (2017).